



UNIVERSITY OF LEEDS

This is a repository copy of *Si-metasomatism in serpentinized peridotite: The effects of talc-alteration on strontium and boron isotopes in abyssal serpentinites from Hole 1268a, ODP Leg 209*.

White Rose Research Online URL for this paper:
<http://eprints.whiterose.ac.uk/80450/>

Version: Submitted Version

Article:

Harvey, J orcid.org/0000-0002-0390-3438, Savov, IP orcid.org/0000-0003-4218-4365, Agostini, S et al. (2 more authors) (2014) Si-metasomatism in serpentinized peridotite: The effects of talc-alteration on strontium and boron isotopes in abyssal serpentinites from Hole 1268a, ODP Leg 209. *Geochimica et Cosmochimica Acta*, 126. pp. 30-48. ISSN 0016-7037

<https://doi.org/10.1016/j.gca.2013.10.035>

Reuse

Items deposited in White Rose Research Online are protected by copyright, with all rights reserved unless indicated otherwise. They may be downloaded and/or printed for private study, or other acts as permitted by national copyright laws. The publisher or other rights holders may allow further reproduction and re-use of the full text version. This is indicated by the licence information on the White Rose Research Online record for the item.

Takedown

If you consider content in White Rose Research Online to be in breach of UK law, please notify us by emailing eprints@whiterose.ac.uk including the URL of the record and the reason for the withdrawal request.



eprints@whiterose.ac.uk
<https://eprints.whiterose.ac.uk/>

1 **Si-metasomatism in serpentized peridotite: the effects of talc-alteration**
2 **on strontium and boron isotopes in abyssal serpentinites from Hole 1268a,**
3 **ODP Leg 209**

4
5 Jason Harvey^{1*}, Ivan P. Savov¹, Samuele Agostini², Robert A. Cliff¹, Richard Walshaw¹

6

7 *1. School of Earth and Environment, University of Leeds, Leeds, LS2 9JT, United Kingdom*

8 *2. Istituto di Geoscienze e Georisorse–CNR, Via Moruzzi 1, 56124 Pisa, Italy*

9

10 For submission to *Geochimica et Cosmochimica Acta*

11

12

13

14

15

16

17

18

19

20

21 *Corresponding author: email feejh@leeds.ac.uk

22 Abstract

23 Ultramafic rocks recovered from Hole 1268a, Ocean Drilling Program Leg 209, to the
24 south of the 15° 20' N Fracture Zone on the Mid-Atlantic ridge have experienced a complex
25 history of melt depletion and subsequent interaction with a series of fluids under varying
26 temperature and pH conditions. After intense melt depletion, varying degrees of
27 serpentinization at 100-200 °C took place, initially under seawater-like pH conditions.
28 Subsequently, interaction with a higher temperature (300-350 °C) fluid with low (4-5) pH
29 and low MgO/SiO₂ resulted in the heterogeneous alteration of these serpentinites to talc-
30 bearing ultramafic lithologies. The proximity of the currently active, high temperature
31 Logatchev hydrothermal field, located on the opposite flank of the Mid-Atlantic ridge,
32 suggests that unlike more distal localities sampled during ODP Leg 209, Hole 1268a has
33 experienced Si-metasomatism (i.e. talc-alteration) by a Logatchev-like hydrothermal fluid.
34 Serpentine strontium isotope ratios were not materially shifted by interaction with the
35 subsequent high-T fluid, despite the likelihood that this fluid had locally interacted with mid-
36 ocean ridge gabbro. ⁸⁷Sr/⁸⁶Sr in the ultramafic lithologies of Hole 1268a are close to that of
37 seawater (c. 0.709) and even acid leached serpentinites retain ⁸⁷Sr/⁸⁶Sr in excess of 0.707,
38 indistinguishable from Logatchev hydrothermal fluid. On the other hand, boron isotope ratios
39 appear to have been shifted from seawater-like values in the serpentinites (δ¹¹B = c. +40 ‰)
40 to much lighter values in talc-altered serpentinites (δ¹¹B = +9 to +20 ‰). This is likely a
41 consequence of the effects of changing ambient pH and temperature during the mineralogical
42 transition from serpentine to talc. Heterogeneous boron isotope systematics have
43 consequences for the composition of ultramafic portions of the lithosphere returned to the
44 convecting mantle by subduction. Inhomogeneities in δ¹¹B, [B] and mineralogy introduce
45 significant uncertainties in the prediction of the composition of slab fluids released during the
46 early- to mid-stages of subduction.

47 **1. Introduction**

48

49 Mid-ocean ridges are responsible for the production of modern-day oceanic
50 lithosphere; material that will, along with pelagic sediments, be re-introduced into the mantle
51 at convergent margins. Around a third of the 55,000 km ridge system is thought to have a full
52 spreading rate of less than 25 mm yr⁻¹ (Dick et al., 2003; Escartín et al., 2003), with the Mid-
53 Atlantic ridge (MAR; Lagabrielle et al., 1998), the Southwest Indian ridge (e.g. Sauter et al.,
54 2004) and the Gakkel ridge in the Arctic Ocean (e.g. Cochran et al., 2003) all containing
55 slow-spreading ridge segments. These segments are often characterized by thin or absent
56 mafic sections, i.e. they are bereft of an igneous crust. Here, peridotite outcrops at the ocean
57 floor and is vulnerable to a wide range of alteration processes such as seafloor weathering
58 (Snow and Dick, 1995) and serpentinization (e.g. Janecky and Seyfried, 1986).

59 Probably the most significant modifications experienced by peridotite at the seafloor
60 are the chemical and mineralogical changes associated with serpentinization. Several studies
61 over the past decade or so have revealed much about the driving forces behind
62 serpentinization reactions. Analyses of vent fluids from peridotite hosted hydrothermal
63 systems (Kelley et al., 2001; Charlou et al., 2002; Douville et al., 2002), petrographic studies
64 (e.g. Mével 2003 and references therein), geochemical investigations (e.g. Paulick et al.,
65 2006; Godard et al., 2008) and the results of experiments and modelling (e.g. Allen and
66 Seyfried, 2003; Foustoukos et al., 2008), have provided valuable insights into the mechanism
67 and chemical consequences of serpentinization at mid-ocean ridges. Primary, anhydrous
68 minerals, such as olivine and orthopyroxene, become hydrated as they are replaced by
69 serpentine minerals (mainly lizardite and chrysotile; e.g. Allen and Seyfried, 2003, but also
70 antigorite, e.g. Kodolányi and Pettke, 2011). Changes in mineral structure associated with the
71 transition from nesosilicates (olivine) and inosilicates (orthopyroxene) to ferro-magnesian

72 phyllosilicates (serpentine minerals) and / or brucite allow the uptake of up to 20 weight %
73 H₂O, although more typically 13-14 wt % H₂O in serpentinites (e.g. Bach et al., 2004;
74 D'Antonio and Kristensen, 2004; Savov et al., 2005) and fluid-mobile elements (e.g. B, Cs,
75 As, I, Br), which can be structurally incorporated into the serpentine crystal lattice (e.g.
76 Scambelluri et al., 2004a; Palmer and Swihart, 1996; Liu and Tossell, 2005; Pabst et al.,
77 2011; Deschamps et al., 2011; Kodolányi et al., 2012), or within the interior of chrysotile
78 scrolls (Wunder et al., 2010). These mineralogical and chemical changes convert a dense,
79 nominally anhydrous, trace element-poor, melt-depleted peridotite protolith into a buoyant,
80 hydrous repository for many trace elements not normally hosted in olivine and
81 orthopyroxene; the minerals that constitute >90% of typical depleted mid-ocean ridge basalt
82 (MORB)-source peridotite. This, in turn, generates a potential geochemical reservoir capable
83 of introducing elemental and isotopic heterogeneity into the sub-arc mantle at active
84 subduction zones and provides an additional source of fluid-mobile elements, over and above
85 that supplied by hydrated meta-basic crust and pelagic sediment, potentially liberated at sub-
86 arc depths (e.g. Morris and Ryan, 2003; Scambelluri et al., 2004b; Savov et al., 2007;
87 Tonarini et al., 2007; Hattori and Guillot, 2007; Deschamps et al., 2011). In addition, the
88 interaction between high-temperature hydrothermal fluid and a serpentinite protolith
89 represents a further opportunity to modify oceanic lithosphere and provide a chemically
90 variable feedstock to the subduction factory in the form of talc (+/- amphibole)-altered
91 serpentinite (e.g. Bach et al., 2004; Paulick et al., 2006; Boschi et al., 2008).

92 Ultramafic-hosted hydrothermal systems have been identified at several locations
93 along amagmatic spreading centres (e.g. Bach et al., 2002). Chemical (e.g. CH₄, Mn) and
94 mid-water light back-scattering anomalies (Charlou et al., 1993; German et al., 1998;
95 Edmonds et al., 2003) suggest that hydrothermal activity at divergent plate margins is
96 commonplace. Ocean Drilling Program Leg 209 recovered significant amounts of

97 serpentinite from five drill sites (Holes 1268a, 1270a, 1271a, 1272a and 1274a) to the north
98 and south of the 15° 20' N fracture zone on the Mid-Atlantic ridge (Shipboard Scientific
99 Party, 2004). Of these, the material recovered from Holes 1272a and 1274a comprise
100 serpentinitized abyssal peridotite (60 to 100 % serpentinitization; Bach et al., 2004). Hole
101 1268a, located c.10 km from the actively venting Logatchev black-smoker hydrothermal field
102 (Batuev et al., 1994; Krasnov et al., 1995; Bogdanov et al., 1997; Shipboard Scientific Party,
103 2004) differs in its mineralogy, bulk rock and mineral geochemistry due to interaction with c.
104 350 °C hydrothermal fluids (Bach et al., 2004; Paulick et al., 2006; Barnes et al., 2009). This
105 study presents a comprehensive assessment of the effects of high-temperature hydrothermal
106 fluid on the composition of a suite of serpentinites. Specifically, new bulk-rock and mineral
107 chemistry and boron and strontium isotope systematics and elemental abundances are used to
108 assess the effects of fluid compositions, fluid / rock ratios, and temperature and pH conditions
109 necessary to transform Hole 1272a- and 1274a-like serpentinites into the talc-bearing
110 lithologies recovered from Hole 1268a. In addition, the implications of subducting such
111 diverse lithospheric material is explored.

112

113 **2. Geological setting and sample petrology**

114

115 The region of the Atlantic Ocean that includes the 15° 20' N fracture zone has been
116 the subject of extensive geophysical (Fujiwara et al., 2003) and submersible surveys (Cannat
117 et al., 1997; Escartín and Cannat, 1999) and has been systematically sampled by dredging and
118 drilling (Cannat et al., 1997; Shipboard Scientific Party, 2004). The flanks either side of the
119 MAR expose serpentinitized peridotite (serpentinite hereafter) and gabbro; the result of
120 extensive crustal thinning on low-angle faults, low magmatic input and the formation of an
121 oceanic core complex (e.g. Ildfonse et al., 2007).

122 Hole 1268a was drilled at 14° 50' N on the western flank of the MAR axial rift; a
123 locality in flat terrain lying upslope of a steep scarp where gabbro-dyke-intruded serpentinites
124 have been identified (Figure 1). Drilling penetrated to a depth of 147.6 metres below sea floor
125 (mbsf) and a total of 78.7 metres of core was recovered. The recovered material comprises
126 harzburgite and dunite that has experienced varying degrees of serpentinization (60 to 100 %)
127 with localized late-stage gabbro/pyroxenite dykes and mylonitic shear zones. The lowermost
128 c. 50 metres, are dominated by microgabbro / gabbronorite that ranges from fresh to highly
129 (40-80 %) altered compositions. (Figure 2; Shipboard Scientific Party, 2004). Details of the
130 samples examined in this study can be found in Table 1. The Logatchev hydrothermal field is
131 located nearby, on the opposite wall of the axial rift at 14° 45' N, within faulted blocks of
132 serpentinite (Figure 1). The presence of strong CH₄ and Mn anomalies in the water column at
133 14° 45' N are indicative of high-temperature interaction between hydrothermal fluid and
134 ultramafic basement (Klinkhammer et al., 1985; Bougault et al., 1993; Rona et al., 1992) and
135 is characterized by the copious outpouring of high-temperature hydrothermal fluid (Schmidt
136 et al. (2007) and references therein).

137 The petrology of Hole 1268a samples has already been discussed extensively
138 (Shipboard Scientific Party, 2004; Bach et al., 2004). The serpentinites have been variably,
139 but extensively (60 to 100 %), serpentinized by hydration of olivine and pyroxene, leading to
140 the formation of serpentine minerals (Seyfried and Dibble, 1980; Seyfried and Ding, 1995;
141 Bach et al., 2004), i.e. “serpentinization *senso stricto*” (Miyashiro et al., 1969; Wicks and
142 Whittaker, 1977; Komor et al., 1985; Janecky and Seyfried, 1986; O'Hanley, 1996). In
143 addition, varying degrees of talc-alteration overprint the serpentinite minerals (e.g.
144 $\text{Mg}_3\text{Si}_2\text{O}_5(\text{OH})_4 + 2\text{SiO}_2(\text{aq}) = \text{Mg}_3\text{Si}_4\text{O}_{10}(\text{OH})_2 + \text{H}_2\text{O}$), a consequence of interaction of
145 serpentinite with a subsequent high-T, low-pH, low-MgO/SiO₂ fluid (Shipboard Scientific
146 Party, 2004; Bach et al., 2004). The intensity of alteration is generally high, with 98-100% of

147 the recovered ultramafic material being serpentinite and / or talc-bearing serpentinite.
148 Serpentinites typically preserve pseudomorphic mesh and hourglass textures, but transitional
149 ribbon textures and non-pseudomorphic interlocking textures are also locally present
150 (Shipboard Scientific Party, 2004; Bach et al., 2004). Evidence for a second period of
151 alteration by a higher temperature (300-350 °C) fluid is preserved in the static overprinting of
152 serpentine structure by talc. This manifests itself as a simple overprint, where earlier textures
153 attributable to serpentinitization are still recognizable, as multiple generations of talc veins
154 cross-cutting predominantly serpentinite areas, and as finely disseminated talc not visible at
155 the hand specimen scale. A comprehensive account of the petrology of Hole 1268a can be
156 found in Shipboard Scientific Party (2004), and the interaction of serpentine with subsequent
157 fluids and the resultant talc alteration are well described in Bach et al. (2004) where these
158 phase relations and textures are particularly well documented (e.g. Figure 3 in Bach et al.,
159 2004). Samples from this study were divided into serpentinites and talc-bearing serpentinites
160 based upon their physical appearance, e.g. obviously talc-bearing on a hand specimen scale,
161 and on their loss on ignition (LOI wt. %, Table S1 in online supplementary material) obtained
162 during major element analyses. Samples with LOI greater than 10 wt. % were deemed to be
163 talc-free, whereas samples with less than 10 wt. % LOI were categorized as talc-bearing,
164 although the low MgO/SiO₂ compared to similar serpentinites suggests that despite their high
165 LOI, samples initially identified as serpentinites may in fact contain finely dispersed talc. In
166 addition, during sample categorization, 3 samples (10R1 35-41, 18R3 87-93 and 19R2 104-
167 110) were found to be chlorite-bearing.

168 In addition to the textural evidence, several lines of geochemical evidence suggest
169 that samples from Holes 1272a and 1274a share a common peridotite protolith with those
170 recovered from Hole 1268a (Shipboard Scientific Party, 2004; Bach et al., 2004; Paulick et
171 al., 2006; Godard et al., 2008). Similarities in major and trace element characteristics of

172 material from Holes 1268a, 1272a and 1274a are consistent with a shared melt-depletion
173 history prior to serpentinization. Low Al_2O_3 (< 1 wt. %) and high bulk rock Mg# (> 91.5;
174 where $\text{Mg\#} = \text{atomic Mg}/(\text{Mg} + \text{Fe}) \times 100$), is consistent throughout the three Holes and
175 indicative of similarly high degrees of melt depletion (Paulick et al., 2006; Godard et al.,
176 2008). On board CO_2 measurements during ODP Leg 209 revealed that talc-altered rocks
177 contain CO_2 of <0.04–0.11 wt. %, which completely overlaps with the serpentine-altered
178 rocks (0.05–0.20 wt. %).

179

180 **3. Analytical methods**

181

182 Based upon observations of recovered core made during ODP Leg 209 and the
183 isotopic, elemental and mineralogical information recorded in previous studies of Hole 1268a
184 (Bach et al., 2004; Paulick et al., 2006; Moll et al., 2007; Barnes et al., 2009), samples were
185 carefully selected from sections of core unaffected by melt infiltration and / or serpentine /
186 talc veining. Surface alteration and potential contamination were removed with a diamond
187 saw followed by repeated rinsing in ultrapure water, prior to drying and powdering in an
188 agate mortar. Whole rock major element abundances were obtained using XRF spectroscopy
189 on a ARL 8420+ dual goniometer wavelength dispersive XRF spectrometer at The Open
190 University and on a PANalytical Axios Advanced XRF spectrometer at the University of
191 Leicester. Major element and Ni data quality were assessed using WS-E and OUG-94 at The
192 Open University and a suite of ultramafic reference materials (including UM-1, UM-2, UM-
193 4, JP-1 and PCC-1) at the University of Leicester. Reproducibility of reference materials is
194 within 2% of recommended values at both laboratories. Loss on ignition was determined by
195 mass difference on powders dried at 110 °C and then fired in a furnace at c. 1000 °C. Mineral
196 major element analyses were performed at the University of Leeds using a Jeol JXL 8230

197 Superprobe. An accelerating voltage of 15 kV was used. Beam currents were typically 15 nA
198 and a beam size of 10 μm was used throughout the study, with reduced beam sizes (4-8 μm)
199 for particularly small areas of talc. Calcium, Mg, Al and Si abundances were all normalized
200 against in-house mineral standards. Reproducibility of all analytical techniques during the
201 course of this study is indistinguishable from the values given in the online supplementary
202 information of Harvey et al. (2010).

203 Strontium was extracted from unleached bulk-rock samples via conventional ion-
204 exchange chromatographic techniques in a clean laboratory facility at the University of
205 Leeds. The total Sr blank was negligible (< 100 pg) compared to the amount of material
206 processed (typically several hundred ng Sr). The analysis of SRM 987 standard during the
207 course of the measurements gave an average $^{87}\text{Sr}/^{86}\text{Sr} = 0.710248 \pm 4$ (2σ ; $n=11$). Prior to
208 dissolution, 4 samples from the uppermost levels of Hole 1268a (2R2 27-35, 2R2 87-93, 4R1
209 44-55, 6R1 100-106) were leached, first with 10 % glacial acetic acid for 15 minutes and then
210 with 1.5M Romil UpA HCl. The leachates and residues were spiked using a highly enriched
211 ^{84}Sr solution before complete dissolution in Romil UpA HNO_3 and UpA HF, before a final
212 dissolution stage in 6M Romil UpA HCl. Strontium was extracted from the leachates and
213 residues using Sr-Spec resin in dilute UpA HNO_3 , before drying prior to analysis by thermal
214 ionisation mass spectrometry (TIMS). Strontium isotope measurements were carried out at
215 the University of Leeds on a Thermo Scientific Triton TIMS instrument running in static
216 mode. The instrumental mass fractionation was corrected for by normalizing results to
217 $^{86}\text{Sr}/^{88}\text{Sr} = 0.1194$. Bulk rock strontium abundances were measured at The Open University
218 using an Agilent 7500a ICP MS after a HF + HNO_3 + HCl digestion. Reference materials
219 PCC-1, BHVO-1 and WS-E were also analysed as a check on reproducibility. Uncertainties
220 on bulk rock Sr abundances are $< 3\%$. Strontium abundances of leached serpentinites and
221 leachates were obtained by isotope dilution, using the same enriched ^{84}Sr spike solution as

222 the respective $^{87}\text{Sr}/^{86}\text{Sr}$ measurements, as part of the strontium isotope ratio determinations.
223 The analytical blank on the Sr abundance measurements were $0.05 \mu\text{g g}^{-1}$.

224 Boron isotopic compositions were measured at IGG (CNR-Pisa, Italy) using a VG
225 Isomass 54E positive ion thermal ionization mass spectrometer following boron extraction
226 and purification procedures described by Tonarini et al. (1997, 2003). The $^{11}\text{B}/^{10}\text{B}$ isotopic
227 ratio is reported in standard delta notation as permil (‰) deviation from the mean value for
228 the SRM-951 boric acid standard routinely passed through the same chemistry as the
229 samples. Precision and accuracy are estimated conservatively as $\pm 0.64 \text{‰}$, based on replicate
230 determinations for samples and for repeated analyses of reference material JB-2 ($\delta^{11}\text{B} = 7.25$
231 $\pm 0.64 \text{‰}$ (2σ), $n=33$ analyses with independent chemistry). Boron abundances were
232 determined on 10 g powder splits by ICP AES following a sodium peroxide digestion at
233 Acme Laboratories, Vancouver, Canada. Duplicate analyses of 6R1 100-106 were within 2
234 $\mu\text{g g}^{-1}$ of each other. Analyses of reference materials LKSD-3 and C3 were within 2 $\mu\text{g g}^{-1}$
235 boron of the certified values. Detection limits of the method are 3 $\mu\text{g g}^{-1}$ boron.

236

237 **4. Results**

238

239 *4.1 Bulk-rock major elements*

240

241 Full bulk-rock major element analyses can be found in Table S1 of the online
242 supplementary electronic material (see also Paulick et al. (2006) for analogous samples).
243 Serpentinized dunites and harzburgites of Sites 1268a typically possess low Al_2O_3
244 abundances ($<1 \text{ wt. \%}$; Table S1). Chlorite-bearing serpentinites 10R1 35-41, 18R3 87-93
245 and 19R2 104-110 and meta-gabbroic samples (27R1 102-109 and 29R1 123-129) contain
246 significantly more Al_2O_3 ; (10-20 wt. % and 15-18 wt. % Al_2O_3 respectively; Table S1).

247 MgO/SiO₂ values of Hole 1268a serpentinites typically fall below the "Terrestrial Array for
248 peridotites" of Jagoutz et al. (1979; MgO/SiO₂ = 0.8 to 1) and are significantly lower than
249 serpentinites from the other side of the 15° 20' N Fracture Zone (e.g. Harvey et al., 2006;
250 Godard et al., 2008). In contrast, talc-altered serpentinites have even lower MgO/SiO₂ values
251 (0.4 - 0.6; Figure 3a), in good agreement with similar samples studied by Paulick et al.
252 (2006). However, it is important to note that *all* of the Hole 1268a serpentinites lie beneath
253 the terrestrial array for peridotite, including serpentinites deemed to have experienced no
254 discernible *macro-scale* talc-alteration (i.e. visible at the hand specimen size). Loss on
255 ignition in Hole 1268a serpentinites is significantly higher (≤ 13 wt. %; Table S1) than that in
256 talc-bearing serpentinites (4-8 wt. %; Table S1), i.e. where the presence of talc is obvious in
257 hand specimen. Two samples (18R3 87-93 and 19R2 104-110) possess >1 wt. % CaO and
258 also elevated TiO₂ (≤ 0.9 wt. %) which suggests that in some isolated samples additional Ca-
259 and / or Ti-bearing phases may occasionally be present, but do not constitute a major part of
260 the altered lithologies. To date, no such phase has been identified petrographically at this
261 locality (Shipboard Scientific Party, 2004; Bach et al., 2004; Paulick et al., 2006; Harvey et
262 al., 2006; Godard et al., 2008; Barnes et al., 2009; this study). The major element
263 compositions of Hole 1268a meta-gabbros from this study are indistinguishable from similar
264 Hole 1268a samples of Paulick et al. (2006). The MgO/SiO₂ and LOI values of Hole 1268a
265 serpentinites and talc-altered serpentinites are also similar to analogous material recovered
266 from further north on the MAR at the Atlantis Massif (Boschi et al., 2008), although meta-
267 gabbros recovered from Atlantis Massif appear somewhat less hydrated and more SiO₂-rich
268 and MgO-poor than at Hole 1268a.

269

270 *4.2 Mineral major element compositions*

271

272 The major element composition of minerals from Hole 1268a serpentinites and talc-
273 bearing serpentinites (Table S2) have already been discussed in detail in Moll et al. (2007),
274 and only an overview of the analogous samples examined as part of this study will be given
275 here. The composition of serpentine after orthopyroxene, serpentine after olivine and talc are
276 indistinguishable from those of Moll et al. (2007) (Figure 3b). Curiously, when analysing
277 minerals that were identified petrographically and by EDS emission spectra as serpentine or
278 talc, quantitative analyses of many secondary minerals were found not to be consistent with
279 the phase initially identified, suggesting that even in samples where bulk-rock LOI indicates a
280 serpentine- or talc-dominated lithology, there is a strong possibility of serpentine-talc
281 intergrowth at a very fine scale. The analyses of Moll et al. (2007) support this assertion, as
282 they also appear to have experienced the same difficulty in unequivocally identifying end-
283 member serpentine and talc. The MgO/SiO_2 vs. $\text{Al}_2\text{O}_3/\text{SiO}_2$ of minerals from both studies are
284 plotted in Figure 3b. Both datasets demonstrate that minerals identified as either serpentine or
285 talc sometimes plot in the compositional field of the other mineral (or occasionally between
286 the two). Only by reducing the analyser beam size (see analytical methods above) were we
287 able to confidently analyse end-member serpentine and talc (Table S2). Chlorite
288 compositions of talc-altered serpentinites have not previously been reported (Table S2). In
289 MgO/SiO_2 vs. $\text{Al}_2\text{O}_3/\text{SiO}_2$ space they are similar to chlorites analysed in serpentinites from
290 Cerro del Almiraz, Spain (Padrón-Navarta et al., 2011; Figure 3b), but are slightly richer in
291 MgO and Al_2O_3 by comparison.

292

293 *4.3 Strontium abundances and isotope analyses*

294

295 Strontium isotope analyses of the various lithologies recovered from Hole 1268a have
296 a wide range of values ($^{87}\text{Sr}/^{86}\text{Sr} = 0.702940 \pm 9$ to 0.71196 ± 15 ; Table 2; Figure 4a). With

297 the exception of the uppermost serpentinite (2R2 27-35; $^{87}\text{Sr}/^{86}\text{Sr} = 0.71196 \pm 15$) unleached
298 serpentinites and talc (\pm chlorite)-altered serpentinites of this study have Sr isotope ratios that
299 are indistinguishable from those of Boschi et al. (2008), where similar lithologies from the
300 MAR were analysed (i.e. $^{87}\text{Sr}/^{86}\text{Sr} = 0.707347 \pm 16$ to 0.709171 ± 13 , Boschi et al., 2008), as
301 were the serpentinites of Delacour et al. (2008) from the same locality ($^{87}\text{Sr}/^{86}\text{Sr} = 0.70885$ to
302 0.70918). The majority of the unleached ultramafic samples from this study have Sr isotope
303 ratios close to that of seawater ($^{87}\text{Sr}/^{86}\text{Sr} = 0.70916$; Palmer and Edmond, 1989),
304 indistinguishable from many of the measurements of Logatchev hydrothermal fluids made by
305 Amini et al. (2008), and also overlap with the Sr isotope ratios obtained by Vils et al. (2009)
306 for variably serpentinized serpentinites from Holes 1272a and 1274a ($^{87}\text{Sr}/^{86}\text{Sr} = 0.70807 \pm 1$
307 to 0.70913 ± 4). There is no correlation between the depth from which the samples were
308 recovered and the Sr isotope ratio (Figure 4a). Similarly, the presence or absence of macro-
309 scale talc-alteration does not appear to be a major control on Sr isotope composition,
310 although two talc (\pm chlorite)-altered samples (18R3 87-93 and 19R2 104-110) possess the
311 lowest Sr isotope ratios of the ultramafic samples of this study.

312 Strontium abundances were determined in eleven serpentinites, nine talc-altered
313 serpentinites and two gabbro-norites. With the exception of the two gabbro samples ($[\text{Sr}] =$
314 72.8 to $86.9 \mu\text{g g}^{-1}$) $[\text{Sr}]$ ranges from 0.41 to $2.44 \mu\text{g g}^{-1}$, with no clear distinction between
315 serpentinite and talc-altered serpentinite (Table 2; Figure 5). While strontium abundances are
316 close to those of similar serpentinite samples reported in Paulick et al. (2006) and Godard et
317 al. (2008), Sr abundances in the serpentinites from this study occupy a much smaller range
318 than those from the Atlantis Massif (up to $15 \mu\text{g g}^{-1}$, Boschi et al., 2008; up to $90 \mu\text{g g}^{-1}$,
319 Delacour et al., 2008). Four samples (2R2 27-35, 2R2 83-89, 4R1 44-55, 6R1 100-106) were
320 sequentially leached first with 10 % glacial acetic acid for 15 minutes and then with 1.5 M
321 HCl for 15 minutes. The results of these leaching experiments can be found in Table S3.

322 Briefly, the combined leaching experiments removed up to 20 % of the original material but
323 account for c. 90 % of the Sr budget. The acetic acid leach liberated a Sr-rich component (50-
324 80 % of the Sr budget) with $^{87}\text{Sr}/^{86}\text{Sr}$ very similar to that of both seawater and the unleached
325 bulk-rock samples. In particular, the anomalously high $^{87}\text{Sr}/^{86}\text{Sr}$ of unleached bulk-rock 2R2
326 27-35 ($^{87}\text{Sr}/^{86}\text{Sr} = 0.71196 \pm 15$) appears to be due to an easily leached component; the acetic
327 acid leach of 2R2 27-35 is very radiogenic compared to the leached residue of that sample
328 ($^{87}\text{Sr}/^{86}\text{Sr} = 0.7172 \pm 8$ vs. 0.70763 ± 3 respectively) and has a relatively high Sr
329 concentration compared to the leached residue ($[\text{Sr}] = 13 \mu\text{g g}^{-1}$ vs. $0.12 \mu\text{g g}^{-1}$ respectively).
330 HCl leaching also removed 10-20 % of the Sr, also with a seawater-like composition
331 ($^{87}\text{Sr}/^{86}\text{Sr} = 0.70901 \pm 1$ to 0.70918 ± 1), leaving a less radiogenic residue in all four cases
332 ($^{87}\text{Sr}/^{86}\text{Sr} = 0.70763 \pm 3$ to 0.70871 ± 6).

333 Two Hole 1268a meta-gabbros were also analysed as part of this study. Samples 27R1
334 102-108 and 29R1 123-129 yielded $^{87}\text{Sr}/^{86}\text{Sr}$ values of 0.702940 ± 9 and 0.703094 ± 11 ,
335 respectively, i.e. only moderately elevated compared to the mean value for MORB recovered
336 north of $17^\circ 10' \text{N}$ on the MAR ($^{87}\text{Sr}/^{86}\text{Sr} = 0.70238 \pm 4$; Dosso et al., 1993).

337

338 *4.4 Boron abundance and isotope analyses*

339

340 Boron abundances were determined on nine serpentinites and six talc-altered
341 serpentinites. Serpentinite boron abundances range from 19 ± 2 to $36 \pm 2 \mu\text{g g}^{-1}$, significantly
342 higher than the talc-altered serpentinites ($[\text{B}] = <3$ to $12 \pm 2 \mu\text{g g}^{-1}$ (Table 3; Figure 5). With
343 the exception of a single talc-altered serpentinite with $[\text{B}]$ of almost $40 \mu\text{g g}^{-1}$, the
344 serpentinites of Boschi et al. (2008) possess similarly high boron abundances when compared
345 to talc-altered serpentinites from the same locality. Boron isotope analyses of Hole 1268a
346 serpentinites and talc (\pm chlorite)-altered samples are presented in Table 3 and illustrated in

347 Figure 4b. Measured values of $\delta^{11}\text{B}$ range from $+9.35 \pm 0.35 \text{ ‰}$ to $+19.56 \pm 0.32 \text{ ‰}$ (where
348 $\delta^{11}\text{B}_{\text{sample}} = ((^{11}\text{B}/^{10}\text{B}_{\text{sample}})/(^{11}\text{B}/^{10}\text{B}_{\text{SRM-951}}) - 1) * 1000$). Similar to the Sr isotope ratios of the
349 same samples, there is no obvious relationship between $\delta^{11}\text{B}$ and depth below seafloor,
350 although the samples with the highest $\delta^{11}\text{B}$ tend to be found towards the lower half of Hole
351 1268a. Again, like the Sr isotope values, there is no clear distinction between talc (\pm
352 chlorite)-altered serpentinites and those that lack macro-scale talc-alteration in terms of $\delta^{11}\text{B}$
353 (Figure 4b). The majority of the ultramafic samples from Hole 1268a overlap in $\delta^{11}\text{B}$ values
354 with serpentinites, talc-altered serpentinites and amphibolite-schists of Boschi et al. (2008),
355 but are considerably lighter than the $\delta^{11}\text{B}$ of Vils et al. (2009) which extend up to $\delta^{11}\text{B} +40$
356 ‰ , i.e. the value of seawater (Foster et al., 2010).

357

358 **5. Discussion**

359

360 A long history of melt depletion is evident in the rocks recovered from ODP Leg 209
361 (Harvey et al., 2006). Extensive serpentinization subsequent to melt depletion, and localized
362 talc-alteration, i.e. Si-metasomatism are also observed. This is indicative of a wide range of
363 pH and temperature conditions during the petrogenesis of the Hole 1268a samples and the
364 evolution of fluid compositions and fluid/rock ratios necessary to induce these characteristics.
365 Any model that explains the boron and strontium isotope systematics must also be consistent
366 with the following observations: (i) the $\delta^{11}\text{B}$ of Hole 1268a samples are consistently lighter
367 than those of Hole 1272a and Hole 1274a, but (ii) are very similar to talc-bearing
368 serpentinites from the Atlantis Massif (Boschi et al., 2008). (iii) There is no clear difference
369 in $\delta^{11}\text{B}$ between the serpentinites and talc-altered serpentinites of Hole 1268a. (iv) The LOI in
370 Hole 1268a samples appears to be bimodal. i.e. there is no continuous variation in the relative

371 proportions of talc and serpentine. In the following sections the evidence for these processes,
372 and the physical and chemical conditions under which they occurred are explored.

373

374 *5.1 The effect of serpentinization and Si-metasomatism on Sr isotope ratios*

375

376 Sequential leaching of the uppermost samples (2R2 27-35 to 6R1 100-106) revealed
377 an easily mobilized component of the Sr budget which, once removed, leaves a residual
378 serpentinite with 1-2 orders of magnitude less Sr and less radiogenic $^{87}\text{Sr}/^{86}\text{Sr}$ than the
379 corresponding unleached serpentinite (Table 2). However, it is evident from Figure 4a that
380 leaching of the uppermost samples from Hole 1268a simply shifts the Sr isotope ratio from
381 values that resemble the unleached samples of Vils et al. (2009) to those of Boschi et al.
382 (2008), also unleached, i.e. although the $^{87}\text{Sr}/^{86}\text{Sr}$ of the leached rocks are noticeably less
383 radiogenic than unleached examples, both unleached and leached samples span a continuum
384 of radiogenic compositions from $^{87}\text{Sr}/^{86}\text{Sr} = c\ 0.707$ to 0.709 , indistinguishable from many of
385 the measurements of Logatchev hydrothermal vent fluids (e.g. Amini et al., 2008). However,
386 it should be noted that the more aggressive HCl leach performed on these samples continued
387 to remove a radiogenic component, which implies that the range of Sr isotope ratios for more
388 aggressively leached samples could be pushed to more unradiogenic values. Notwithstanding
389 this observation, the source of the easily-leachable Sr is somewhat equivocal. On board
390 measurements during ODP Leg 209 revealed that talc-altered rocks contain CO_2 of <0.04 –
391 0.11 wt. %, which completely overlaps with the serpentinites (0.05 – 0.20 wt. %). In the
392 serpentinites that lack macro-scale talc-alteration a positive correlation is evident between
393 CO_2 and H_2O (Shipboard Scientific Party, 2004). However, a general absence of carbonate
394 veining (Bach et al., 2011) and the lack of any significant correlation between volatile content
395 and depth below sea floor suggests that late-stage carbonate formation is unlikely to be

396 responsible for the readily leached, seawater-like Sr reservoir ($^{87}\text{Sr}/^{86}\text{Sr}$ seawater = 0.70916;
397 Palmer and Edmond, 1989). The presence of an easily leachable Sr component also has some
398 implications for calculated water / rock ratios necessary to account for the observed
399 alteration.

400 Water / rock ratios (W/R) were calculated for the Hole 1268a samples using the
401 "single pass" model employed by Vils et al. (2009), which is based upon, and uses the same
402 parameters as Taylor (1977) and McCulloch et al. (1980). The highly melt depleted protolith
403 has particularly low [Sr] ($1.75 \mu\text{g g}^{-1}$; Harvey et al., 2006; Paulick et al., 2006; Godard et al.,
404 2008; Vils et al., 2009; Barnes et al., 2009). Mixing calculations suggest that the
405 transformation of peridotite to a serpentinite with seawater-like Sr isotopic characteristics
406 requires only low W/R (2-8 for the Hole 1268a samples) due to the low Sr concentration in
407 highly depleted serpentinite compared to seawater. Bearing in mind that the structurally
408 bound Sr constitutes only a small percentage of the Sr budget of unleached samples (<20 %),
409 and the process of near complete serpentinization shifted $^{87}\text{Sr}/^{86}\text{Sr}$ of unleached samples to
410 values of c. 0.709 then the calculated W/R ratios for Hole 1268a can be considered a
411 maximum.

412 The Hole 1268a serpentinites, calculated to have experienced relatively low W/R
413 ratios compared to Hole 1272a and Hole 1274a serpentinites (cf. Vils et al., 2009), appear to
414 possess a radiogenic Sr isotope composition despite interaction with the later high-
415 temperature hydrothermal fluid. This, in itself, is curious. It is inferred that the high-
416 temperature fluid with which serpentinite must have interacted to produce talc-bearing rocks
417 had acquired its high-Si composition through interaction with local gabbro (Bach et al., 2004;
418 Paulick et al., 2006; Barnes et al., 2009). Given that relatively unaltered gabbros from Hole
419 1268a retain a mantle-like Sr isotope ratio and contain 1-2 orders of magnitude more Sr than
420 the serpentinites ($^{87}\text{Sr}/^{86}\text{Sr}$ = 0.702940 to 0.703094, [Sr] = 73 to 87 $\mu\text{g g}^{-1}$; this study),

421 interaction between serpentinite, with a seawater-like Sr isotope ratio, and a high
422 temperature, high-Si fluid that has partially broken down MORB-like gabbro should quickly
423 reduce the $^{87}\text{Sr}/^{86}\text{Sr}$ of the talc-altered serpentinites. Indeed, strontium isotope ratios as low as
424 $^{87}\text{Sr}/^{86}\text{Sr} = 0.70477$ have been recorded in Logatchev hydrothermal fluids (Amini et al.,
425 2008), suggesting that some fluids have equilibrated more completely with the local gabbro
426 than others, but $^{87}\text{Sr}/^{86}\text{Sr}$ as low as this appears to be exceptional. The majority of Sr that
427 could be derived from the gabbro is plagioclase-hosted and it is not clear whether plagioclase
428 alteration is synchronous with the breakdown of orthopyroxene, i.e. it is not certain that the
429 Sr-rich fluid released during plagioclase breakdown was also the source of the high-Si
430 signature. There are several possible explanations for why the final talc-altered Sr isotope
431 ratio is not significantly reduced (i.e. to values of < 0.707 in leached samples, or < 0.709 in
432 unleached samples) by interaction with the high-Si, high-T fluid. Preferential breakdown of
433 orthopyroxene versus plagioclase would minimize the amount of unradiogenic Sr released
434 during the hydrothermal alteration of gabbro, while still releasing sufficient SiO_2 to produce
435 the necessary seawater-Sr-dominated, high-Si fluid. Alternatively, hydrothermal interaction
436 with a previously altered gabbro, i.e. one that has interacted with large volumes of seawater,
437 and whose plagioclase has acquired a seawater-like Sr isotope signature, may subsequently
438 provide a high temperature fluid with a more radiogenic Sr isotope ratio, which would not
439 necessarily dramatically lower the $^{87}\text{Sr}/^{86}\text{Sr}$ of the final talc-altered serpentinite, although this
440 would require highly altered plagioclase to co-exist with relatively unaltered orthopyroxene.
441 Core descriptions of gabbro from ODP Leg 209 (Shipboard Scientific Party, 2004) show that
442 plagioclase in Core 27R1 to 29R1 is largely unaltered, whereas orthopyroxene is often
443 completely replaced. This favours the former explanation for the lack of a drastic reduction in
444 $^{87}\text{Sr}/^{86}\text{Sr}$ (i.e. < 0.707) during Si-metasomatism; even if unradiogenic Sr is hosted within the
445 unaltered orthopyroxene this mineral is not a significant source of Sr. However, it should be

446 noted that on a local scale, the degree of alteration of the gabbro is not homogeneous and
447 likely to be the result of local heterogeneity in available fluid pathways, i.e. one of these "end
448 member" hypotheses is unlikely to account for all the Sr isotope systematics of all the Hole
449 1268a serpentinites.

450 Based upon our interpretations, we can propose the following scenarios to account for
451 the observed Sr isotope systematics. (i) Serpentinization of a highly melt-depleted peridotite
452 protolith results in a serpentinite with Sr isotope characteristics similar to seawater, after Sr
453 exchange at low W/R ratios. (ii) Limited exchange of Sr between serpentinite and a
454 subsequent high-Si, high temperature fluid with a mantle-like Sr isotope ratio lowers the
455 serpentinite $^{87}\text{Sr}/^{86}\text{Sr}$ to values similar to those observed in leached serpentinites (i.e. \leq
456 $^{87}\text{Sr}/^{86}\text{Sr}$ 0.707). (iii) Late-stage interaction with seawater near to the surface of the seafloor
457 adds an easily-leachable, i.e. not structurally bound, seawater-like Sr component that
458 dominates the bulk-rock Sr budget and returns the bulk-rock Sr isotope ratio to seawater-like
459 values ($^{87}\text{Sr}/^{86}\text{Sr} \sim 0.709$). Despite requiring a three-step process this seems the most likely
460 sequence of events as it does not rely upon the simultaneous release of Si from orthopyroxene
461 with the retention of most of the gabbro-bearing Sr in unaltered plagioclase.

462

463 *5.2 The effects of serpentinization and Si-metasomatism on B isotope systematics*

464

465 This study benefits from the prior knowledge of B and Sr isotope systematics of a
466 local, likely precursor to talc-altered serpentinite - the material recovered from Hole 1272a
467 and 1274a (Shipboard Scientific Party, 2004; Bach et al., 2004; Paulick et al., 2006; Godard
468 et al., 2008; Vils et al. 2009; Barnes et al., 2009). The $\delta^{11}\text{B}$ values of Hole 1272a and 1274a
469 serpentinites (Vils et al., 2009), range from seawater-like, where seawater $\delta^{11}\text{B} = +39.61 \pm$
470 0.04 ‰ ; Foster et al. (2010) to a $\delta^{11}\text{B}$ of c.+30 ‰, significantly heavier than the samples of

471 this study ($\delta^{11}\text{B} = +9$ to $+20$ ‰) (Table 3). However, irrespective of lithology, the Hole
472 1268a samples yield $\delta^{11}\text{B}$ values that are close to the range of the talc-altered serpentinites
473 described by Boschi et al. (2008) with $\delta^{11}\text{B}$ values of $+9$ to $+16$ ‰, who interpreted the $\delta^{11}\text{B}$
474 of the Atlantis Massif talc-serpentinites as being the result of an interaction with a moderate
475 temperature (c. 250 °C) fluid under mostly open system conditions and highly variable W/R
476 ratios (0.5 to > 100). From Figure 4b it can be seen that the Hole 1272a and 1274a
477 serpentinites have much higher $\delta^{11}\text{B}$ than the 1268a samples and those from the Atlantis
478 Massif. This suggests that the $\delta^{11}\text{B}$ of serpentinites and talc-altered serpentinites of Hole
479 1268a are the result of a multi-stage alteration process at this locality, where low temperature
480 (100 - 200 °C) serpentinization raised $\delta^{11}\text{B}$ (and $^{87}\text{Sr}/^{86}\text{Sr}$) to seawater-like values before a
481 subsequent high temperature event reduced the B isotope ratio of the serpentinites and talc-
482 altered serpentinites, while leaving Sr isotope ratios largely unaffected. This contrasts with
483 the scenario described by Boschi et al. (2008) for the Atlantis Massif talc-bearing
484 serpentinites where serpentine and talc generation was synchronous.

485 The speciation of boron in a fluid is strongly dependent upon pH, with alkaline
486 conditions being favourable for boron removal from solution (Foustoukos et al., 2008; Figure
487 6a). At low temperature (0 - 25 °C) and at seawater pH (7.5 to 8.4) c. 80 % of boron in a
488 seawater-like solution is trigonally coordinated (Figure 6a), with the remainder being
489 tetrahedrally coordinated (Hemming and Hanson, 1992). The models of Benton et al. (2001)
490 and Boschi et al. (2008) demonstrate that continuing increases in fluid pH at moderate
491 temperatures (c. 250 °C) during the uptake of boron by serpentine minerals results in heavy,
492 trigonally coordinated boron and the incorporation of ^{11}B -rich tetrahedrally coordinated
493 boron into serpentine minerals (Figure 6b). With their calculated fluid-mineral fractionation
494 factors Boschi et al. (2008) calculate that a solution dominated by trigonally coordinated
495 boron with $\delta^{11}\text{B}$ of c. $+55$ to $+60$ ‰, i.e. in equilibrium with serpentine minerals dominated

496 by tetrahedrally coordinated boron with $\delta^{11}\text{B}$ of c. +40 ‰, is attained for solutions at c. 250
497 °C at a pH of c. 10. This is consistent with the measured $\delta^{11}\text{B}$ of Hole 1272a and 1274a
498 serpentinites (Vils et al., 2009) and broadly consistent with the "single pass" model for fluid-
499 rock interaction (Vils et al., 2009).

500 It has been clearly demonstrated that during the changes in mineralogy associated
501 with low-temperature alteration and serpentinization B is rapidly accumulated in
502 phyllosilicates (Pabst et al., 2011), increasing both the $\delta^{11}\text{B}$ and [B] as serpentinization
503 progresses (e.g. Wunder et al., 2005). This accounts for the high [B] and $\delta^{11}\text{B}$ of the
504 serpentinites of Hole 1272a and 1274a as reported by Vils et al. (2008, 2009, respectively)
505 (Figure 6a). By way of contrast, the high-T, high-Si fluid associated with talc-alteration has
506 been calculated to have had a pH of 4 to 5 (Bach et al., 2004). Under these pH conditions B is
507 entirely trigonally coordinated with little propensity for incorporation of ^{11}B into tetrahedrally
508 coordinated sites within the stable mineral phases. Thus any B incorporated during changes in
509 mineralogy will have a much lower $\delta^{11}\text{B}$ than minerals formed under higher pH conditions
510 (Figure 6b). The net effect is a pH-controlled fractionation that differs markedly from the
511 prevailing conditions during low temperature serpentinization (Figure 6b). As trigonally
512 coordinated B is less easily incorporated into silicates (e.g. Williams et al., 2001), otherwise
513 identical minerals will have lower boron abundances and $\delta^{11}\text{B}$ than minerals formed at high
514 pH. This is consistent with the offset to lower $\delta^{11}\text{B}$ in talc-altered serpentinites of this study
515 and those from the Atlantic Massif (Boschi et al., 2008), and also the lower [B] measured in
516 talc-altered serpentinites versus low-temperature serpentinites (Boschi et al., 2008 vs. Vils et
517 al., 2008, respectively).

518 Superimposed upon the pH-influenced fluid-mineral fractionation of $\delta^{11}\text{B}$ is an
519 additional temperature effect (Figure 6b). As predicted from Figure 6b, the maximum fluid-
520 mineral fractionation of B isotopes occurs at the lowest pH. Although the fluids associated

521 with Si-metasomatism at Hole 1268a are likely to have been in the region of pH 4 to 5, the
522 maximum fluid-mineral fractionation occurs at a pH of c. 6, where all B present is trigonally
523 speciated; a further reduction on fluid pH has no additional effect on fluid-mineral
524 fractionation. Similarly, the maximum degree of fluid-mineral B isotope fractionation occurs
525 at low temperatures (Figure 6b). With increasing temperature the potential range of fluid-
526 mineral induced fractionation contracts. However, at the temperatures associated with Si-
527 metasomatism (300 to 350 °C; Bach et al., 2004; Paulick et al., 2006) and pH of <6 there
528 remains the potential for a significant fluid-mineral fractionation of B isotopes during the
529 talc-alteration of pre-existing serpentine. Figure 6b demonstrates that under the conditions of
530 Si-metasomatism at Hole 1268a this could have been as great as -19 ‰; a degree of
531 fractionation that encompasses most of the differences observed between the serpentinites
532 from Hole 1272a and 1274a ($\delta^{11}\text{B} = +29.72$ to $+40.66$ ‰; Vils et al., 2009) and talc-altered
533 serpentinites of this study ($\delta^{11}\text{B} = +9.65$ to $+19.56$ ‰) and from the Atlantis Massif ($\delta^{11}\text{B} =$
534 $+8.78$ to $+16.21$ ‰; Boschi et al., 2008). Moreover, this large degree of fluid-mineral
535 fractionation is only possible at the low pH associated with Si-metasomatism. The
536 synchronous occurrence of serpentinization during talc-alteration would buffer the low pH of
537 the silicic high-T fluid and thus restrict the possible range of fractionation of boron isotopes
538 to a value below that observed in the Hole 1268a serpentinites.

539

540 *5.3 The consequences of mineralogical changes during serpentinization and subsequent Si-* 541 *metasomatism*

542

543 The multi-stage evolution of the 1268a talc-altered serpentinites is summarized in
544 Figure 7. Changes in [Sr], [B], $\delta^{11}\text{B}$ and $^{87}\text{Sr}/^{86}\text{Sr}$ during the sequential transition from melt
545 depleted peridotite to serpentine to talc-altered serpentine are not only controlled by fluid

546 composition and ambient pH-T conditions, but also the change in mineralogy during the
547 evolution of the Hole 1268a material. Melt-depleted peridotite lithologies are dominated by
548 olivine and orthopyroxene with simple nesosilicate and inosilicate orthorhombic structures,
549 respectively. Their structures are not conducive to large-scale substitution of major cations by
550 Sr and / or B, hence the low abundances of these elements in peridotitic lithologies (e.g. [Sr]
551 and [B] in the primitive mantle are estimated at $20 \mu\text{g g}^{-1}$ and $<0.25 \mu\text{g g}^{-1}$ respectively;
552 Palme and O'Neill, 2003; Chaussidon and Jambon, 1995, respectively). In contrast, the
553 ferromagnesian, phyllosilicate serpentine $[\text{Mg}_3\text{Si}_2\text{O}_5(\text{OH})_4]$ is a trioctahedral sheet silicate
554 comprising stacked layers of a pseudo-hexagonal network of linked SiO_4 tetrahedra
555 interspersed with brucite-like $[\text{Mg}(\text{OH})_2]$ layers (Deer et al. 1992). Thus, there is a much
556 greater potential for the incorporation of Sr and / or B either within the pseudo-hexagonal
557 network itself, or between the sheets during the process of serpentinization, which in turn
558 accounts for the large differences in B and Sr systematics between unaltered mafic-ultramafic
559 material and serpentinites (e.g., Bonatti et al. 1984; Ryan and Langmuir 1993; Benton et al.
560 2001; Snyder et al. 2005; Vils et al. 2008, 2009; Deschamps et al. 2010; Pabst et al., 2011).
561 Melt-depleted peridotite which still retains its mantle-like Sr and B isotope signatures
562 ($^{87}\text{Sr}/^{86}\text{Sr} = 0.7025$ e.g. Hofmann, 1997; $\delta^{11}\text{B} = \text{c. } -5 \text{‰}$, e.g. Chaussidon and Marty, 1995) is
563 systematically serpentinized through interaction with a high-pH, seawater-dominated fluid.
564 The inherently low [Sr] (1 to $3 \mu\text{g g}^{-1}$, Paulick et al., 2006; Godard et al., 2008) and
565 especially low [B] ($0.06 \mu\text{g g}^{-1}$, Salters and Stracke, 2004) of the melt depleted peridotite
566 means that $\delta^{11}\text{B}$ in particular will rapidly shift to heavier $\delta^{11}\text{B}$ with increased seawater /
567 peridotite interaction. Simple binary mixing calculations demonstrate that during
568 serpentinization a depleted peridotite pre-cursor will acquire seawater-like $\delta^{11}\text{B}$ after
569 interacting with c. 10 % of the fluid necessary to impart seawater Sr isotopic characteristics
570 (Figure 7). However, this is reliant upon certain assumptions regarding the uptake of B into

571 the serpentinizing peridotite, i.e. the trajectory assumed in Figure 7 for the change in both B
572 and Sr isotope systematics relies upon the rapid uptake of B by serpentine minerals and the
573 complete exchange of B between the serpentine phases and seawater. Pabst et al. (2011)
574 demonstrate that there is strong evidence for incorporation of B into the serpentine mineral
575 structure itself. The mechanism of B incorporation into serpentine is independent of the
576 serpentine polymorph or textural type (e.g., Pelletier et al. 2008; Pabst et al., 2011). Highly
577 charged ($+3$) B should be readily accommodated within the Si and / or Al crystallographic
578 sites. For example in both chlorite-group and mica-group minerals, B^{3+} either partly replaces
579 Al in tetrahedral coordination ($[4]Al^{3+}$) (Foord et al. 1991; Zagorsky et al. 2003), or enters the
580 $[4]Si^{4+}$ site (Ranoroso et al. 1989). From these observations, Pabst et al. (2011) hypothesize
581 that B is directly incorporated into the serpentine crystal structure in tetrahedral coordination.
582 Thus, the rate of increase of [B] and $\delta^{11}B$ is likely to be dependent upon kinetics of serpentine
583 production rather than a simple W/R ratio calculation with an assumed 100 % exchange of B
584 between the fluid and the rock undergoing serpentinization. Vils et al. (2009) clearly showed
585 that there is no straightforward relationship between degree of serpentinization and either [B]
586 or $\delta^{11}B$. Under open system conditions, where the supply of seawater-derived B is effectively
587 unlimited, the supply of B to rapidly serpentinizing peridotite is unlikely to be a limiting
588 factor. As both Boschi et al. (2008) and Vils et al. (2009) note, there is a significant fluid-
589 mineral fractionation factor under these pH-T conditions (Figure 6b). At some point, in order
590 to produce serpentine minerals with seawater-like $\delta^{11}B$, closed system distillation of seawater
591 must occur (Vils et al., 2009), with pH evolving over time from seawater-like pH to the high
592 pH (c.10) necessary to incorporate heavy $\delta^{11}B$ ($\delta^{11}B = c. +40 \text{ ‰}$) in serpentine minerals. In
593 essence, if serpentinization commenced under open-system conditions it would appear that it
594 culminated under closed system conditions.

595 It is clear that there is a marked offset in $\delta^{11}\text{B}$ of up to 20 ‰ between the Hole 1272a
596 and Hole 1274a serpentinites of Vils et al. (2009) and the Hole 1268a samples. As discussed
597 above, Hole 1268a samples have Sr isotope ratios that are indistinguishable from those of
598 Hole 1272a and Hole 1274a. Furthermore, both leached and unleached Hole 1268a samples
599 overlap completely with the serpentinites and talc-altered serpentinites of Boschi et al.
600 (2008), suggesting that 75-100 ‰ of the peridotite-protolith Sr budget has been exchanged
601 with seawater-derived Sr. Where these two sample suites appear to differ is in the acquisition
602 of the final $\delta^{11}\text{B}$ signature in both serpentinites and talc-altered serpentinites, which is
603 probably related to the differences in the exact settings of the two localities, despite their
604 seemingly similar mid-ocean ridge locations.

605 Serpentinites contain significantly more B than talc-altered serpentinites (Boschi et
606 al., 2008; Vils et al., 2008, 2009; this study Table 3) so whatever mechanism is responsible
607 for the shift from seawater-like $\delta^{11}\text{B}$ to significantly lighter values must also account for the
608 evident decrease in boron abundance and be consistent with the mechanisms that account for
609 the observed Sr isotope systematics. Pabst et al. (2011) observe that boron hosted along grain
610 boundaries, in microfractures, or in between serpentine sheets, would be removed by
611 infiltrating hydrous fluids irrespective of temperature. However, this highly mobile
612 component is not likely to affect the overall B systematics of serpentine to any great extent.
613 In addition, Pabst et al. (2011) report that serpentine mesh centres and mesh rims contain by
614 far the most B in lizardite-dominated serpentinite lithologies (up to $197 \mu\text{g g}^{-1}$ and $97 \mu\text{g g}^{-1}$
615 respectively), i.e. the majority of serpentine-hosted B is structurally bound and can only be
616 extracted as a result of serpentine recrystallization, breakdown through changes in P-T-X
617 conditions, or significant shifts in fluid pH (e.g., Palmer et al. 1987; Spivack and Edmond
618 1987; Ulmer and Trommsdorff 1995; Hawthorne et al. 1996; Palmer and Swihart 1996;
619 Peacock and Hervig 1999; Hattori and Guillot 2003; Schmidt et al. 2005).

620 The pervasive talc-alteration / Si-metasomatism present throughout the Hole 1268a
621 samples of this study is clear evidence for a mineralogical change in response to the presence
622 of a high-T, low-pH fluid (Bach et al. 2004; Paulick et al., 2006). The change from a tri-
623 octahedral sheet silicate (serpentine) with relatively high MgO/SiO₂ to monoclinic / triclinic
624 talc with a distinctly lower MgO/SiO₂ requires a significant re-ordering of the crystal
625 structures. This has the potential to not only allow B to be removed from formerly
626 structurally bound ^[4]Al³⁺ and ^[4]Si⁴⁺ sites during recrystallization but is also accompanied by a
627 dehydration reaction where the amount of structurally bound water is reduced from up to 14
628 wt. % in serpentine (Vils et al., 2009; this study) to 4-8 wt. % in talc-bearing serpentinites
629 (Boschi et al., 2008; this study). As boron is considered to be a particularly fluid-mobile
630 element (e.g. Ryan and Langmuir, 1993; Palmer and Swihart, 1996; Ryan et al., 1996;
631 Ishikawa and Tera, 1997; Savov et al., 2007) this presents a viable mechanism for the
632 reduction in [B] during the transition from serpentine to talc-altered serpentine. Moreover,
633 the change in fluid composition relative to that responsible for serpentinization (higher T,
634 lower pH, higher Si content) induces a fluid-mineral fractionation that is distinctly different
635 to that induced during serpentinization. For example, Figure 6b illustrates that at c.350 °C
636 and in the presence of a fluid of pH 6, mineral compositions can be shifted to δ¹¹B c. 10 ‰
637 lighter than the results of interaction with a seawater-like fluid at 200 °C. This does not take
638 into account any differences in the actual starting composition of the higher temperature fluid
639 which may (or may not) have a distinctly lighter δ¹¹B than the lower temperature
640 serpentinizing fluid. However, it seems unlikely that the higher temperature fluid would
641 possess a heavier δ¹¹B than the earlier serpentinizing fluid, given the evidence presented by
642 Vils et al. (2009) suggesting that closed-system refinement of fluid composition is required in
643 order to precipitate serpentine minerals with δ¹¹B of c. +40 ‰.

644 Despite strong evidence for a significant dehydration event, and the likely
645 fractionation of boron that accompanied the transition from serpentine to talc, the apparent
646 lack of offset in $\delta^{11}\text{B}$ between the Hole 1268a serpentinites and the talc-bearing serpentinites
647 needs to be reconciled with the theoretical framework discussed above. All of the Hole 1268a
648 samples plot below the Terrestrial Array for peridotite (Figure 3a), implying that at least
649 some shift to a lower MgO/SiO_2 has occurred through interaction with the late-stage high-
650 temperature Si-bearing fluid. Despite this observation, many Hole 1268a samples retain high
651 LOI values, which suggests that while some talc may be present in all of the Hole 1268a
652 samples, in serpentinites where talc has not been observed on a macro-scale it may only be
653 present in small amounts as a micron-scale intergrowth with serpentine. This is consistent
654 with the apparent difficulty in identifying talc-free serpentine during electron microprobe
655 analyses (Moll et al., 2007; this study). For all of the Hole 1268a samples to shift from
656 seawater-like $\delta^{11}\text{B}$ (cf. Vils et al., 2009) to those observed in this study (and those of Boschi
657 et al., 2008), implies that the $\delta^{11}\text{B}$ of serpentinite changes almost completely at the onset of
658 talc formation and that significant further changes in $\delta^{11}\text{B}$ are unlikely with increasing
659 degrees of talc growth. In this case, at least, the dominant factor controlling the $\delta^{11}\text{B}$ may be
660 the different fluid-mineral fractionation that prevails at low-pH and high-temperature, acting
661 in concert with a fluid produced under open-system conditions. This fluid has not
662 experienced the in-situ distillation process described by Vils et al. (2009) necessary to
663 produce particularly heavy $\delta^{11}\text{B}$ in minerals and provides a source of lighter $\delta^{11}\text{B}$ than that
664 with which the serpentinite lithologies of Hole 1272a and 1274a were in equilibrium.

665 This also helps to reconcile the measured B isotope ratios with the suggested
666 sequence of events that account for the Sr isotope systematics of the Hole 1268a samples.
667 The return to seawater-like Sr isotope signatures through interaction with seawater at ocean
668 floor ambient conditions is not mimicked by the boron isotope systematics because, at the

669 low temperatures at the surface of the seafloor, fluid-mineral fractionation of boron isotopes
670 will be at a maximum. Any boron incorporated into mineral phases under these conditions
671 will be particularly light. For example, at pH 8.2 and at temperatures of <100 °C, fluid-
672 mineral fractionation factors would be at least -24 ‰ (Figure 6b), resulting in a shift in
673 mineral hosted B to $\delta^{11}\text{B} = +16 \text{ ‰}$ (assuming equilibrium with seawater with $\delta^{11}\text{B} +40 \text{ ‰}$)
674 which is in good agreement with the measured values of Hole 1268a samples.

675

676 *5.4 Implications of talc-bearing lithologies at convergent margins.*

677

678 The significance of talc-bearing ultramafic lithologies exhumed at convergent
679 margins has been recognised for decades. Hydration of the mantle wedge (e.g. Bebout and
680 Barton, 1989; Fryer et al., 1999; Marschall and Schumacher, 2012), generation of chemical
681 and isotopic heterogeneity in the mantle wedge (e.g. Gerya and Yuen 2003; Hyndman and
682 Peacock, 2003; Grove et al., 2009), and erosion, entrainment and transport of heterogeneous
683 serpentinite and its derivatives have resulted in lively debate regarding the ultimate fate of
684 boron-bearing lithologies contained within the downgoing slab versus that removed from the
685 mantle wedge through subduction erosion (e.g. Peacock and Hervig, 1999; Benton et al.,
686 2001; Savov et al., 2005; Tonarini et al., 2011; Scambelluri and Tonarini, 2012; Marschall
687 and Schumacher, 2012). Despite the lower boron concentrations in talc compared to
688 serpentinite (Boschi et al., 2008; Vils et al., 2008), the stability of talc to greater depths and
689 higher pressures during subduction (Pawley and Wood, 1995) has the potential for the
690 delivery of boron, sometimes isotopically lighter than its precursor serpentinite (cf. Boschi et
691 al., 2008; Vils et al., 2009; this study), to deeper regions beneath evolving arcs, and possibly
692 even beyond the arc in cold subduction zones.

693 The talc-altered serpentinites of ODP Leg 209 Hole 1268a represent a rare example of
694 serpentinite that has been recently and variably altered by interaction with a high-T, low-pH,
695 high-Si fluid at a mid-ocean ridge setting. Although likely restricted to areas of mid-ocean
696 ridges that are experiencing mid- to high-temperature hydrothermal activity, such as the area
697 around the Logatchev hydrothermal field, processes such as those observed during this study
698 may occur in many spreading centre settings where anomalous concentrations of CH₄, H₂ and
699 / or Mn are detected, or mid-water light back scattering anomalies are observed in the
700 overlying water column. While the generation and subduction of talc-bearing serpentinite
701 produced as a result of prograde metamorphism is well known at convergent margins (e.g.
702 Sorensen and Grossman, 1993; Bebout and Barton, 2002; King et al., 2003, 2007; Spandler et
703 al., 2008; Marschall and Schumacher, 2012) little effort has been dedicated to the
704 quantification of the effects of subducting talc generated at mid-ocean ridge settings. This is
705 inevitably a function of the (im)practicalities of sampling peridotite at mid-ocean ridges and
706 the lack of knowledge regarding the abundance and spatial extent of these lithologies. As
707 more information is gathered regarding the distribution of high-temperature, ultramafic-
708 hosted hydrothermal systems, then the relative contributions of convergent-margin- versus
709 mid-ocean ridge-generated talc to boron transport at, and beyond, subduction zones will
710 become clearer.

711

712 **6. Concluding remarks**

713

714 The ultramafic samples recovered from Hole 1268a, ODP Leg 209 have experienced
715 high degrees of prior melt depletion, most of which occurred in antiquity, followed by
716 multiple episodes of fluid / rock interaction and hydrothermal alteration. The sequential
717 transformation from melt-depleted peridotite to serpentinite to talc-altered serpentinite has

718 imparted distinctive $\delta^{11}\text{B}$ signatures, similar to talc-altered serpentinites seen elsewhere on
719 the Mid-Atlantic ridge. Assuming that serpentinites from nearby Hole 1272a and Hole 1274a
720 are reasonable analogues for Hole 1268a lithologies, a likely sequence of events can be
721 constructed to account for the present day boron and strontium isotope systematics of Hole
722 1268a serpentinites and talc-bearing serpentinites. Low temperature (c. 200 °C) interaction
723 with seawater resulted in intense to complete serpentinization of a nominally anhydrous
724 peridotite protolith, accompanied by a shift in $\delta^{11}\text{B}$ to seawater-like values and a shift in Sr
725 isotope ratios to significantly more radiogenic values. Subsequent interaction with a high-
726 temperature (300-350 °C), low-pH, Si-bearing hydrothermal fluid induced varying degrees of
727 talc-alteration, i.e. Si-metasomatism, causing a shift to lighter $\delta^{11}\text{B}$ (likely accompanied by a
728 significant loss of boron) but no significant change in Sr isotope systematics. Although talc
729 formation under these conditions results in an ultramafic lithology with a reduced boron
730 concentration compared to serpentinite, it potentially provides a feedstock to subduction
731 zones with a more variable, and lighter $\delta^{11}\text{B}$ than previously expected based upon the
732 subduction of serpentinite.

733

734 **Acknowledgements**

735

736 We would like to thank John Watson and Nick Marsh for assistance with the XRF
737 measurements. This manuscript benefitted from thoughtful reviews by Horst Marschall,
738 Fabien Deschamps and a third anonymous reviewer. We would particularly like to thank
739 Richard Walker for his patient editorial handling. This research used samples provided by the
740 Ocean Drilling Program (ODP). ODP is sponsored by the U.S. National Science Foundation
741 and participating countries under the management of the Joint Oceanographic Institutions
742 (JOI) Inc.

743 **References**

744

745 Allen, D. E., Seyfried, W. E. J., (2003). Compositional controls on vent fluids from
746 ultramafic-hosted hydrothermal systems at mid-ocean ridges: An experimental study at
747 400 °C, 500 bars. *Geochim. Cosmochim. Acta*, **67** (8), 1531–1542.

748

749 Amini, M., Eisenhauer, A., Böhm, F., Fietzke, J., Bach, W., Garbe-Schönberg, D., Rossner,
750 M., Bock, B., Lackschewitz, K. S., Hauff, F., (2008). Calcium isotope ($\delta^{44/40}\text{Ca}$)
751 fractionation along hydrothermal pathways, Logatchev field (Mid-Atlantic Ridge, 14°-
752 45'N). *Geochim. Cosmochim. Acta* **72**, 4107-4122, doi:10.1016/j.gca.2008.05.055.

753

754 Bach, W., Banerjee, N. R., Dick, H. J. B., Baker, E. T., (2002). Discovery of ancient and
755 active hydrothermal systems along the ultra-slow spreading Southwest Indian Ridge 10°–
756 16° E. *Geochem. Geophys. Geosyst.* **3**, doi:10.1029/2001GC000279.

757

758 Bach, W., Garrido, C. J. Paulick, H., Harvey, J., Rosner, M., (2004). Seawater-peridotite
759 interactions: First insights from ODP Leg 209, MAR 15°N. *Geochem. Geophys. Geosyst.*
760 **5**, doi:10.1029/2004GC000744.

761

762 Bach, W., Rosner, M., Jöns, N., Rausch, S., Robinson, L. F., Paulick, H., Erzinger, J., (2011).
763 Carbonate veins trace seawater circulation during exhumation and uplift of mantle rock:
764 Results from ODP Leg 209. *Earth Planet. Sci. Lett.* **311**, 242-252.

765

766 Barnes, J. D., Paulick, H., Sharp, Z. D., Bach, W., Beaudoin, G., (2009). Stable isotope
767 ($\delta^{18}\text{O}$, δD , $\delta^{37}\text{Cl}$) evidence for multiple fluid histories in mid-Atlantic abyssal peridotites
768 (ODP Leg 209). *Lithos* **110**, 83–94, doi:10.1016/j.lithos.2008.12.004.

769

770 Batuev, B. N., Krotov, A. G., Markov, V. F., Cherkashov, G. A., Krasnov, S., Lisitsin, Y. D.,
771 (1994). Massive sulfide deposits discovered and sampled at 14°45'N, Mid-Atlantic Ridge.
772 *BRIDGE Newsl.* **6**, 6–10.

773

774 Bebout, G. E., Barton, M. D., (1989). Fluid flow and metasomatism in a subduction zone
775 hydrothermal system: Catalina schist terrane, California. *Geology* **17**, 976-980.

776

777 Bebout, G. E., Barton, M. D., (2002). Tectonic and metasomatic mixing in a high-T,
778 subduction-zone melange; insights into the geochemical evolution of the slab-mantle
779 interface. *Chem. Geol.* **187** (2), 79-106.

780

781 Benton, L. D., Ryan, J. G., Tera, F., (2001). Boron isotope systematics of slab fluids as
782 inferred from a serpentine seamount, Mariana forearc. *Earth Planet. Sci. Lett.* **187**, 273–
783 282.

784

785 Bogdanov, Y. A., Bortnikov, N. S., Vikentyev, I. V., Gurvich, E. G., Sagalevich, A. M.,
786 (1997). A new type of modern mineral-forming system: black smokers of the
787 hydrothermal field at 14°45' N Latitude, Mid-Atlantic Ridge. *Geol. Ore Depos.* **39**, 58–78.

788

789 Bonatti, E., Lawrence, J. R., Morandi, N., (1984). Serpentinization of oceanic peridotites:
790 temperature dependence of mineralogy and boron content. *Earth Planet. Sci. Lett.* **70**, 88–
791 94.

792

793 Boschi, C., Dini. A., Früh-Green, G. L., Kelley, D. S., (2008). Isotopic and element exchange
794 during serpentinization and metasomatism at the Atlantis Massif (MAR 30°N): Insights
795 from B and Sr isotope data. *Geochim. Cosmochim. Acta* **72**, 1801–1823.

796

797 Bougault, H., Charlou, J. L., Fouquet, Y., Needham, H. D., Vaslet, N., Appriou, P., Baptiste,
798 P. J., Rona, P. A., Dmitriev, L., Silantiev, S., (1993). Fast and slow spreading ridges:
799 Structure and hydrothermal activity, ultramafic topography highs, and CH₄ output. *J.*
800 *Geophys. Res.* **98**, 9643–9651.

801

802 Cannat, M., Lagabrielle, Y., de Coutures, N., Bougault, H., Casey, J. Dmitriev, L. Fouquet,
803 Y., (1997). Ultramafic and gabbroic exposures at the Mid-Atlantic Ridge: Geological
804 mapping in the 15°N region. *Tectonophys.* **279**, 193–213.

805

806 Charlou, J. L., Bougault, H., Appriou, P., Nelsen, T., Rona, P. A., (1993). Different
807 TDM/CH₄ hydrothermal plume signatures: TAG site at 26°N and serpentinized ultrabasic
808 diapir at 15°05'N on the Mid-Atlantic Ridge. *Geochim. Cosmochim. Acta* **55**, 3209–3222.

809

810 Charlou, J. L., Donval, J.- P., Fouquet, Y., Jean-Baptiste, P., Holm N., (2002). Geochemistry
811 of high H₂ and CH₄ vent fluids issuing from ultramafic rocks at the Rainbow hydrothermal
812 field (36°14'N, MAR). *Chem. Geol.* **191**, 345–359.

813

814 Chaussidon, M., Jambon, A. (1994). Boron content and isotopic composition of oceanic
815 basalts: Geochemical and cosmochemical implications. *Earth Planet. Sci. Lett.* **121**, 277-
816 291.

817

818 Chaussidon, M., Marty B., (1995). Primitive boron isotope composition of the mantle.
819 *Science* **269**, 383–386.

820

821 Cochran, J. R., Kurras, G. J., Edwards, M. H., Coakley, B. J., (2003). The Gakkel Ridge;
822 bathymetry, gravity anomalies and crustal accretion at extremely slow spreading rates. *J.*
823 *Geophys. Res.* **108** (B2), doi:10.1029/2002JB001830.

824

825 D'Antonio, M., Kristensen, M. B., (2004). Serpentine and brucite of ultramafic clasts from
826 the South Chamorro Seamount (Ocean Drilling Program Leg 195, Site 1200): inferences
827 for the serpentinization of the Mariana fore-arc mantle. *Min. Mag.* **68**, 887-904.

828

829 Deer, W. A., Howie, R. A., Zussman, J., (1992). An Introduction to the Rock-Forming
830 Minerals. Longman Scientific and Technical, New York.

831

832 Delacour, A., Früh-Green, G. L., Frank, M., Gutjahr, M., Kelley, D. S., (2008). Sr- and Nd-
833 isotope geochemistry of the Atlantis Massif (30°N, MAR): Implications for fluid fluxes
834 and lithospheric heterogeneity. *Chem. Geol.* **254**, 19-35,
835 doi:10.1016/j.chemgeo.2008.05.018.

836

837 Deschamps, F., Guillot, S., Godard, M., Chauvel, C., Andreani, M., Hattori, K., (2010). In
838 situ characterization of serpentinites from forearc mantle wedges: Timing of

839 serpentinitization and behavior of fluid-mobile elements in subduction zones. *Chem. Geol.*
840 **269**, 262–277, doi:10.1016/j.chemgeo.2009.10.002.

841

842 Deschamps, F., Guillot, S., Godard, M., Andreani, M., Hattori, K., (2011). Serpentinites act
843 as sponges for fluid-mobile elements in abyssal and subduction zone environments.
844 *Terra Nova* **23**, 171–178. doi: 10.1111/j.1365-3121.2011.00995.x.

845

846 Dick, H. J. B., Lin, J., Schouten, H., (2003). An ultraslow-spreading class of ocean ridge.
847 *Nature* **426**, 405–412.

848

849 Dosso, L., Bougault, H., Joron, J.-L., (1993). Geochemical morphology of the North Mid-
850 Atlantic Ridge, 10°–24°N: Trace element-isotope complementarity. *Earth Planet. Sci.*
851 *Lett.* **120**, 443–462.

852

853 Douville, E., Charlou, J. L., Oelkers, E. H., Bianvenu, P., Jove Colon, C. F., Donval, J. P.,
854 Fouquet, Y., Prieur, D., Appriou, P., (2002). The rainbow vent fluids (36° 14' N, MAR):
855 The influence of ultramafic rocks and phase separation on trace metal contents on Mid-
856 Atlantic Ridge hydrothermal fluids. *Chem. Geol.* **184**, 37–48.

857

858 Edmonds, H. N., Michael, P. J., Baker, E. T., Connelly, D. P., Snow, J., Langmuir, C. H.,
859 Dick, H. J. B., Mühe, R., German, C. R., Graham, D. W., (2003). Discovery of abundant
860 hydrothermal venting on the ultra-slow spreading Gakkel ridge in the Arctic Ocean.
861 *Nature* **421**, 252–256.

862

863 Escartín, J., Cannat, M., (1999). Ultramafic exposures and the gravity signature of the
864 lithosphere near the Fifteen-Twenty Fracture Zone (Mid-Atlantic Ridge, 14°–16.5°N).
865 *Earth Planet. Sci. Lett.* **171**, 411–424.

866

867 Escartín, J., Mével, C., Macleod, C. J., McCaig, A. M., (2003). Constraints on deformation
868 conditions and the origin of oceanic detachments, the Mid-Atlantic Ridge core complex at
869 15° 45' N. *Geochem., Geophys., Geosys.* **4**, doi:10.1029/2002GC000472.

870

871 Foord, E. E., Martin, R. F., Fitzpatrick, J. J., Taggart, J. E., Crock, J. G. Jr., (1991).
872 Boromuscovite, a new member of the mica group, from the Little Three mine pegmatite,
873 Ramona district, San Diego County, California. *Am. Mineral.* **76**, 1998–2002.

874

875 Foster, G. L., Pogge von Strandmann, P. A. E., Rae, J. W. B., (2010) Boron and magnesium
876 isotopic composition of seawater. *Geochem., Geophys., Geosys.* **11**, doi:
877 10.1029/2010GC003201.

878

879 Foustoukos, D. I., Savov, I. P., Janecky, D. R., (2008). Chemical and isotopic constraints on
880 water/rock interactions at the Lost City hydrothermal field, 30° N Mid-Atlantic Ridge.
881 *Geochim. Cosmochim. Acta* **72**, 5457-5474.

882

883 Fryer, P., Wheat, C. G., Mottl, M. J., (1999). Mariana blueschist mud volcanism implications
884 for conditions within the subduction zone. *Geology* **13**, 103-106.

885

886 Fujiwara, T., Lin, J., Matsumoto, T., Kelemen, P. B., Tucholke, B. E., Casey, J. F., (2003).
887 Crustal evolution of the Mid-Atlantic Ridge near the Fifteen-Twenty Fracture Zone in the
888 last 5 Ma. *Geochem. Geophys. Geosyst.* **4**, 1024, doi:10.1029/2002GC000364.
889

890 German, C. R., Baker, E. T., Mével, C., Tamaki, K., Fuji Scientific. Team, (1998).
891 Hydrothermal activity along the southwest Indian ridge. *Nature* **395**, 490–493.
892

893 Gerya, T. V., Yuen, D. A., (2003). Rayleigh-Taylor instabilities from hydration and melting
894 propel ‘cold plumes’ at subduction zones. *Earth Planet. Sci. Lett.* **212**, 47–62,
895 doi:10.1016/S0012-821X(03)00265-6.
896

897 Godard, M., Lagabriele, Y., Alard, O., Harvey, J., (2008). Geochemistry of the highly
898 depleted peridotites drilled at ODP Sites 1272 and 1274 (Fifteen–Twenty Fracture Zone,
899 Mid-Atlantic Ridge): implications for mantle dynamics beneath a slow spreading ridge.
900 *Earth Planet. Sci. Lett.* **267**, 410–425, doi:10.1016/j.epsl.2007.11.058.
901

902 Grove, T. L., Till, C. B., Lev, E., Chatterjee, N., Medard, E., (2009). Kinematic variables and
903 water transport control the formation and location of arc volcanoes. *Nature* **459**, 694–697,
904 doi:10.1038/nature08044.
905

906 Harvey, J., Gannoun, A., Burton, K. W., Rogers, N. W., Alard, O., Parkinson, I. J., (2006).
907 Ancient melt extraction from the oceanic upper mantle revealed by Re–Os isotopes in
908 abyssal peridotites from the Mid-Atlantic ridge. *Earth Planet. Sci. Lett.* **244**, 606–621,
909 doi:10.1016/j.epsl.2006.02.031.
910

911 Harvey J., Gannoun A., Burton K. W., Rogers N. W., Schiano P., Alard O., (2010).
912 Unravelling the effects of melt depletion and secondary infiltration on mantle Re–Os
913 isotopes beneath the French Massif Central. *Geochim. Cosmochim. Acta* **74**, 293–320,
914 doi:10.1016/j.gca.2009.09.031.
915

916 Harvey, J., Yoshikawa, M., Hammond, S. J., Burton, K. W., (2012). Deciphering the trace
917 element characteristics in Kilbourne Hole peridotite xenoliths: melt-rock interaction and
918 metasomatism beneath the Rio Grande Rift, SW USA. *J. Petrol.* **53** (8), 1709-1742.
919 doi:10.1093/petrology/egs030.
920

921 Hattori, K. H., Guillot, S., (2003). Volcanic fronts form as a consequence of serpentinite
922 dehydration in the forearc mantle wedge. *Geology* **31**, 525–528.
923

924 Hattori, K., Guillot, S., (2007). Geochemical character of serpentinites associated with high-
925 to ultrahigh-pressure metamorphic rocks in the Alps, Cuba, and the Himalayas:
926 Recycling of elements in subduction zones. *Geochem. Geophys. Geosys.* **8** (9) Q09010.
927 doi:10.1029/2007GC001594.
928

929 Hawthorne, Y., Burns, P., Grice, J., (1996). The crystal chemistry of boron. In E.S. Grew,
930 Ed., Boron: Mineralogy, petrology, and geochemistry, 33, p. 41–116. Reviews in
931 Mineralogy, Mineralogical Society of America, Chantilly, Virginia.
932

933 Hemming, N. G., Hanson, G. N., (1992). Boron isotopic composition and concentration in
934 modern marine carbonates. *Geochim. Cosmochim. Acta* **56**, 537-543.
935

936 Hofmann, A.W., (1997). Mantle geochemistry: the message from oceanic volcanism. *Nature*
937 **385**, 219-229.

938

939 Hyndman, R. D., Peacock, S. M., (2003). Serpentinization of the forearc mantle. *Earth*
940 *Planet. Sci. Lett.* **212**, 417–432, doi:10.1016/S0012-821X(03)00263-2.

941

942 Ildefonse, B., Blackman, D. K., John, B. E., Ohara, Y., Miller, D. J., MacLeod, C. J.,
943 Integrated Ocean Drilling Program Expeditions 304/305 Science Party, (2007). Oceanic
944 core complexes and crustal accretion at slow-spreading ridges. *Geology* **35**, 623–626; doi:
945 10.1130/G23531A.1.

946

947 Ishikawa, T., Tera, F., (1997). Source, composition and distribution of fluid in the Kurile
948 mantle wedge: constraints from across-arc variations of B/Nb and B isotopes. *Earth*
949 *Planet. Sci. Lett.* **152**, 123–138.

950

951 Jagoutz, E., Palme, H., Baddenhausen, H., Blum, K., Cendales, M., Dreibus, G., Spettel, B.,
952 Lorenz, V., Waenke, H., (1979). The abundances of major, minor and trace elements in
953 the Earth's mantle as derived from primitive ultramafic nodules. In: Proceedings of the
954 Lunar and Planetary Science Conference, vol. 2 (eds. R. B. Merrill, D. D. Bogard, F.
955 Hoerz, D. S. McKay and P. C. Robertson). Pergamon, New York, pp. 2031–2050.

956

957 Janecky, D. R., Seyfried Jr., W. E., (1986). Hydrothermal serpentinization of peridotite
958 within the oceanic crust: Experimental investigations of mineralogy and major element
959 chemistry. *Geochim. Cosmochim. Acta* **50**, 1357–1378.

960

961 Kelley, D. S., Karson, J. A., Blackman, D. K., Früh-Green, G. L., Butterfield, D. A., Lilley,
962 M. D., Olson, E. J., Schrenk, O. M., Roe, K. K., Lebon, G. T., Rivizzigno, P., AT3-60
963 Shipboard Party, (2001). An off-axis hydrothermal vent field near the Mid-Atlantic Ridge
964 at 30° N. *Nature* **412**, 145–149.

965

966 King, R. L., Kohn, M. J., Eiler, J. M., (2003). Constraints on the petrologic structure of the
967 subduction zone slab-mantle interface from Franciscan Complex exotic ultramafic blocks.
968 *Geol. Soc. Am. Bull.* **115**, 1097–1109.

969

970 King, R. L., Bebout, G. E., Grove, M., Moriguti, T., Nakamura, E., (2007). Boron and lead
971 isotope signatures of subduction-zone mélange formation: Hybridization and fractionation
972 along the slab-mantle interface beneath volcanic arcs. *Chem. Geol.* **239**, 305-322.

973

974 Klinkhammer G., Rona, P., Greaves, M., Elderfield, H., (1985). Hydrothermal manganese
975 plumes in the Mid-Atlantic Ridge rift valley. *Nature* **314**, 727-731 doi:10.1038/314727a0.

976

977 Kodolányi, J., Pettke, T., (2011). Loss of trace elements from serpentinites during fluid-
978 assisted transformation of chrysotile to antigorite - An example from Guatemala. *Chem.*
979 *Geol.* **284**, 351–362.

980

981 Kodolányi, J., Pettke, T., Spandler, C., Kamber, B. S., Gméling, K., (2012). Geochemistry of
982 Ocean Floor and Fore-arc Serpentinites: Constraints on the Ultramafic Input to Subduction
983 Zones. *J. Petrol.* **53** (2), 235-270 doi:10.1093/petrology/egr058.

984

985 Komor, S. C., Elthon, D., Casey, J. F., (1985). Serpentinization of cumulate ultramafic rock
986 from the North Arm Mountain massif of the Bay of Islands ophiolite. *Geochim.*
987 *Cosmochim. Acta* **49**, 2331–2338.

988

989 Krasnov, S. G., Cherkashev, G. A., Stepanova, T. V., Batuyev, B. N., Krotov, A. G., Malin,
990 B. V., Maslov, M. N., Markov, V. F., Poroshina, I. M., Samovarov, M. S., Ashadze, L.
991 I., Lazareva, A. M., Ermolayev, I. K., (1995). Detailed geological studies of hydrothermal
992 fields in the North Atlantic, in *Hydrothermal Vents and Processes*. Eds: Parson, L. M.,
993 Walker, C. L., Dixon, D. R. *Geol. Soc. Spec. Publ.* **87**, 43–64.

994

995 Lagabrielle, Y., Bideau, D., Cannat, M., Karson, J. A., Mével, C., (1998). Ultramafic–mafic
996 plutonic rock suites exposed along the Mid-Atlantic Ridge (10°N–30°N)-symmetrical
997 asymmetrical distribution and implications for seafloor spreading processes. In: Buck, W.
998 R., Delaney, P. T., Karson, J. A., Lagabrielle, Y. (Eds.), *Faulting and magmatism at mid*
999 *ocean ridges. AGU Geophysical Monograph* **106**, pp. 153–176.

1000

1001 Liu, Y., Tossell, A., (2005). Ab initio molecular orbital calculations for boron isotope
1002 fractionations on boric acids and borates. *Geochim. Cosmochim. Acta* **69**, 3995–4006.

1003

1004 Marschall, H. R., Schumacher, J. C. (2012). Arc magmas sourced from mélange diapirs in
1005 subduction zones. *Nature Geosci.* **5**, 862–867. doi: 10.1038/ngeo1634.

1006

1007 McCulloch, M., Gregory, R. T., Wasserburg, G. J., Taylor, H. P. J., (1980). A neodymium,
1008 strontium and oxygen isotopic study of the cretaceous Semail ophiolite and implications

1009 for the petrogenesis and seawater-hydrothermal alteration of oceanic crust. *Earth Planet.*
1010 *Sci. Lett.* **46**, 201–211.

1011

1012 Mével, C., (2003). Serpentinization of abyssal peridotite at mid-ocean ridges. *C. R. Geosci.*
1013 **335**, 825–852.

1014

1015 Miyashiro, A., Shido, F., Ewing, M., (1969). Composition and origin of serpentinites from
1016 the Mid-Atlantic Ridge near 24° and 30° north latitude. *Contrib. Mineral. Petrol.* **23**, 117–
1017 127.

1018

1019 Moll, M., Paulick, H., Suhr, G., Bach, W., (2007). Data report: microprobe analyses of
1020 primary phases (olivine, pyroxene, and spinel) and alteration products (serpentine, iowaite,
1021 talc, magnetite, and sulfides) in Holes 1268A, 1272A, and 1274A. In Kelemen, P.B.,
1022 Kikawa, E., and Miller, D.J. (Eds.), *Proc. ODP, Sci. Results* **209**, College Station, TX
1023 (Ocean Drilling Program), 1–13. doi:10.2973/odp.proc.sr.209.003.2007.

1024

1025 Morris, J. D., Ryan, J. G., (2003). Subduction zone processes and implications for changing
1026 composition of upper and lower mantle. *Treatise on Geochemistry*, **2** (11), 451-470.

1027

1028 O'Hanley, D. S., (1996). Serpentinites - records of tectonic and petrological history. *Oxford*
1029 *Monographs on Geology and Geophysics* **34**. Oxford University Press. 277 pp.

1030

1031 Pabst, S., Zack, T., Savov, I. P., Ludwig, T., Rost, D., Vicenzi, E. P., (2011). Evidence for
1032 boron incorporation into the serpentine crystal structure. *Am. Mineral.* **96**, 1112-1119.

1033

1034 Padrón-Navarta, J. - A., López Sánchez-Vizcaíno, V., Garrido, C. J., Gómez-Pugnaire, M. T.,
1035 (2011). Metamorphic record of high-pressure dehydration of antigorite-serpentinite to
1036 chlorite-harzburgite in a subduction setting (Cerro del Almirez, Nevado-Fílabride
1037 complex, southern Spain. *J. Petrol.* **52** (10), 2047-2078, doi:10.1093/petrology/egr039.
1038

1039 Palme, H., O'Neill, H. St. J., (2003). Cosmochemical estimates of mantle composition.
1040 *Treatise on Geochemistry* **2** (1), 1-38.
1041

1042 Palmer, M. R., Edmond, J., (1989). The strontium isotope budget of the modern ocean. *Earth*
1043 *Planet. Sci. Lett.* **92**, 11–26.
1044

1045 Palmer, M. R., Swihart, G. H., (1996). Boron isotope geochemistry: an overview. In E.S.
1046 Grew, and I.M. Anovitz, Eds., Boron: Mineralogy, Petrology and Geochemistry, 33, p.
1047 709–744. *Reviews in Mineralogy*, Mineralogical Society of America, Chantilly, Virginia.
1048

1049 Palmer, M. R., Spivack, A. J., Edmond, J. M., (1987). Temperature and pH controls over
1050 isotopic fractionation during adsorption of boron on marine clay. *Geochim. Cosmochim.*
1051 *Acta* **51**, 2319–2323.
1052

1053 Paulick, H, Bach, W., Godard, M., De Hoog, J. C. M., Suhr, G., Harvey, J., (2006).
1054 Geochemistry of abyssal peridotites (Mid-Atlantic Ridge, 15°20'N, ODP Leg 209):
1055 Implications for fluid/rock interaction in slow spreading environments. *Chem. Geol.* **234**,
1056 179–210, doi:10.1016/j.chemgeo.2006.04.011.
1057

1058 Pawley, A. R., Wood, B. J., (1995). The high-pressure stability of talc and 10 A° phase:
1059 potential storage sites for H₂O in subduction zones. *Am. Mineral.* **80**, 998–1003.
1060

1061 Peacock, S. M., Hervig, R. L., (1999). Boron isotopic composition of subduction-zone
1062 metamorphic rocks. *Chem. Geol.* **160**, 281–290.
1063

1064 Pelletier, L., Müntener, O., Kalt, A., Vennemann, T. W., Belgya, T., (2008). Emplacement of
1065 ultramafic rocks into the continental crust monitored by light and other trace elements: An
1066 example from the Geisspfad body (Swiss-Italian Alps). *Chem. Geol.* **255**, 143–159, doi:
1067 10.1016/j.chemgeo.2008.06.024.
1068

1069 Ranoroso, N., Fontan, F., Fransolet, A. M., (1989). Rediscovery of manandonite in the
1070 Sahatany Valley, Madagascar. *Eur. J. Mineral.* **1**, 633–638.
1071

1072 Rona, P. A., Bougault, H., Charlou, J. L., Appriou, P., Nelsen, T. A., Trefry, J. H., Eberhart,
1073 G. L. A., Barone, P. A., Needham, H. D., (1992). Hydrothermal circulation,
1074 serpentinization, and degassing at a rift valley—fracture zone intersection: Mid-Atlantic
1075 Ridge near 15°N, 45°W. *Geology* **20**, 783–786.
1076

1077 Ryan, J. G., Langmuir, C. H., (1993). The systematics of boron abundances in young
1078 volcanic-rocks. *Geochim. Cosmochim. Acta* **57**, 1489–1498.
1079

1080 Ryan, J. G., Leeman, W. P., Morris, J. D., Langmuir, C. H., (1996). The boron systematics of
1081 intraplate lavas: Implications for crust and mantle evolution. *Geochim. Cosmochim. Acta*
1082 **60**, 415–422.

1083

1084 Salters, V. J. M., Stracke, A., (2004). Composition of the depleted mantle. *Geochem.*
1085 *Geophys. Geosys.* **5**, doi: 10.1029/2002GC000347.

1086

1087 Sauter, D., Mendel, V., Rommevaux-Jestin, C., Parson, L. M., Fujimoto, H., Mével, C.
1088 Cannat, M., Tamaki, K., (2004). Focused magmatism versus amagmatic spreading along
1089 the ultra-slow spreading Southwest Indian Ridge: evidence from TOBI side sonar
1090 imagery. *Geochem., Geophys., Geosys.* **5**, 1–20, Q10K09, doi: 10.1029/2004GC000738.

1091

1092 Savov, I. P., Ryan, J. G., D'Antonio, M., Kelly, K., Mattie, P., (2005). Geochemistry of
1093 serpentized peridotites from the Mariana Forearc Conical Seamount, ODP Leg 125:
1094 Implications for the elemental recycling at subduction zones. *Geochem. Geophys. Geosyst.*
1095 **6**, Q04J15, doi:10.1029/2004GC000777.

1096

1097 Savov, I. P., Ryan, J. G., D'Antonio, M., Fryer, P., (2007). Shallow slab fluid release across
1098 and along the Mariana arc-basin system: Insights from geochemistry of serpentized
1099 peridotites from the Mariana Forearc. *J. Geophys. Res.* **112**, B09205.
1100 doi:10.1029/2006JB004749.

1101

1102 Scambelluri, M., Tonarini, S., (2012). Boron isotope evidence for shallow fluid transfer
1103 across subduction zones by serpentized mantle. *Geology* **40**, 907-910,
1104 doi:10.1130/G33233.1.

1105

1106 Scambelluri, M., Fiebig, J., Malaspina, N., Müntener, O., Pettke T., (2004a). Serpentinite
1107 Subduction: Implications for Fluid Processes and Trace-Element Recycling. *Int. Geol.*
1108 *Rev.* **46** (7), 595-613 doi: 10.2747/0020-6814.46.7.595.

1109

1110 Scambelluri, M., Müntener, O., Ottolini, L., Pettke, T. T., Vannucci, R., (2004b). The fate of
1111 B, Cl and Li in the subducted oceanic mantle and in the antigorite breakdown fluids. *Earth*
1112 *Planet. Sci. Lett.* **222**, 217–234.

1113

1114 Schmidt, C., Thomas, R., Heinrich, W., (2005). Boron speciation in aqueous fluids at 22 to
1115 600 °C and 0.1 MPa to 2 GPa. *Geochim. Cosmochim. Acta* **69**, 275–281.

1116

1117 Schmidt, K., Koschinsky, A., Garbe-Schönberg, D., de Carvalho, L. M., Seifert, R., (2007).
1118 Geochemistry of hydrothermal fluids from the ultramafic-hosted Logatchev hydrothermal
1119 field, 15°N on the Mid-Atlantic Ridge: Temporal and spatial investigation. *Chem. Geol.*
1120 **242**, 1–21, doi:10.1016/j.chemgeo.2007.01.023.

1121

1122 Seyfried, W. E., Dibble, W. E. J., (1980). Sea water - peridotite interaction at 300 °C and 500
1123 bars: Implications for the origin of oceanic serpentinites. *Geochim. Cosmochim. Acta* **44**,
1124 309–321.

1125

1126 Seyfried, W. E., Ding, K., (1995). Phase equilibria in subsea floor hydrothermal systems: A
1127 review of the role of redox, temperature, pH and dissolved Cl on the chemistry of hot
1128 spring fluids on mid-ocean ridges, in Seafloor Hydrothermal Systems: Physical, Chemical,
1129 Biological and Geological Interactions, *Geophys. Monogr. Ser.* **91**, Eds. S. E. Humphris et
1130 al., pp. 248–272, AGU, Washington, D. C.

1131

1132 Shipboard Scientific Party, (2004). Leg 209 summary. In: Kelemen, P.B., Kikawa, E., Miller,
1133 D.J., et al. (Eds.), *Proc. ODP, Init. Repts.* **209** College Station TX, pp. 1–139.

1134

1135 Snow, J. E., Dick, H. J. B., (1995). Pervasive magnesium loss by marine weathering of
1136 peridotite. *Geochim. Cosmochim. Acta* **59**, 4219–4235.

1137

1138 Snyder, G. T., Savov, I. P., Muramatsu, Y., (2005). Iodine and boron in Mariana serpentinite
1139 mud volcanoes (ODP Legs 125 and 195): Implications for forearc processes and
1140 subduction recycling. In M. Shinohara, M. H. Salisbury, and C. Richter, Eds., *Proc. ODP.*
1141 *Sci. Res.* **195**, 1–18.

1142

1143 Spandler, C., Hermann, J., Faure, K., Mavrogenes, J. A., Arculus, R. J., (2008). The
1144 importance of talc and chlorite “hybrid” rocks for volatile recycling through subduction
1145 zones; evidence from the high-pressure subduction mélange of New Caledonia. *Contrib.*
1146 *Mineral. Petrol.* **155**, 181-198, doi: 10.1007/s00410-007-0236-2.

1147

1148 Spivack, A. J., Edmond, J. M., (1987). Boron isotope exchange between seawater and the
1149 oceanic crust. *Geochim. Cosmochim. Acta* **51**, 1033–1043.

1150

1151 Sorensen, S. S., Grossman, J. N., (1993). Accessory minerals and subduction zone
1152 metasomatism: a geochemical comparison of two mélanges (Washington and California,
1153 U.S.A.). *Chem. Geol.* **110**, 269–297.

1154

1155 Taylor, H. P. J., (1977). Water/rock interactions and the origin of H₂O in granitic batholiths.
1156 *J. Geol. Soc. (London)* **133**, 509–558.
1157

1158 Tonarini, S., Pennisi, M., Leeman, W. P., (1997). Precise boron analysis of complex silicate
1159 (rock) samples using alkali carbonate fusion and ion exchange separation. *Chem. Geol.*
1160 **142**, 129–137.
1161

1162 Tonarini, S., Pennisi, M., Adorni-Braccesi, A., Dini, A., Ferrara, G., Gonfiantini, R.,
1163 Wiedenbeck, M., Gröning, M., (2003). Intercomparison of boron isotope and
1164 concentration measurements: Part I: Selection, preparation and homogeneity tests of the
1165 intercomparison materials. *Geostand. Newslett.* **27**, 21–39.
1166

1167 Tonarini, S., Agostini, S., Doglioni, C., Innocenti, F., Manetti, P., (2007). Evidence for
1168 serpentinite fluid in convergent margin systems: The example of El Salvador (Central
1169 America) arc lavas. *Geochem. Geophys. Geosys.* **8** (9), Q09014,
1170 doi:10.1029/2006GC001508.
1171

1172 Tonarini, S., Leeman, W. P., Leat, P. T., (2011). Subduction erosion of forearc mantle wedge
1173 implicated in the genesis of the South Sandwich Island (SSI) arc: Evidence from boron
1174 isotope systematics. *Earth Planet. Sci. Lett.* **301**, 275–284, doi:10.1016/j.epsl.2010.11.008.
1175

1176 Ulmer, P., Trommsdorff, V., (1995). Serpentinite stability to mantle depths and subduction-
1177 related magmatism. *Science* **268**, 858–861.
1178

1179 Vils, F., Pelletier, L., Kalt, A., Müntener, O., Ludwig, T., (2008). The Lithium, Boron and
1180 Beryllium content of serpentinized peridotites from ODP Leg 209 (Sites 1272A and
1181 1274A): Implications for lithium and boron budgets of oceanic lithosphere. *Geochim.*
1182 *Cosmochim. Acta* **72**, 5475–5504.

1183

1184 Vils, F., Tonarini, S., Kalt, A., Seitz, H. - M., (2009). Boron, lithium and strontium isotopes
1185 as tracers of seawater–serpentinite interaction at Mid-Atlantic ridge, ODP Leg 209. *Earth*
1186 *Planet. Sci. Lett.* **286**, 414–425.

1187

1188 Wicks, F. J., Whittaker, E. J. W., (1977). Serpentinite textures and serpentinization. *Can.*
1189 *Mineral.* **15**, 459–488.

1190

1191 Williams, L. B., Hervig, R. L., Holloway, J. R., Hutcheon, I., (2001). Boron isotope
1192 geochemistry during diagenesis. Part I. Experimental determination of fractionation during
1193 illitization of smectite. *Geochim. Cosmochim. Acta* **65**, 1769–1782.

1194

1195 Wunder, B., Meixner, A., Romer, R. L., Wirth, R., Heinrich, W., (2005). The geochemical
1196 cycle of boron: constraints from boron isotope partitioning experiments between mica and
1197 fluid. *Lithos* **84**, 206-216.

1198

1199 Wunder, B., Deschamps, F., Watenphul, A., Guillot, S., Meixner, A., Romer, R. L., Wirth, R.
1200 (2010). The effect of chrysotile nanotubes on the serpentine-fluid Li-isotopic fractionation.
1201 *Contrib. Mineral. Petrol.* **159**, 781-790 doi: 10.1007/s00410-009-0454-x.

1202

1203 Yalçın, H, Bozkaya, Ö., (2006). Mineralogy and geochemistry of Palaeocene ultramafic- and
1204 sedimentary-hosted talc deposits in the southern part of the Sivas basin, Turkey. *Clay and*
1205 *Clay Minerals* **54** (3), 333-350.

1206

1207 Zagorsky, V. Y., Peretyazhko, I. S., Sapozhnikov, A. N., Zhukhlistov, A. P., and Zvyagin, B.
1208 B., (2003). Borocookeite, a new member of the chlorite group from the Malkhan gem
1209 tourmaline deposit, Central Transbaikalia, Russia. *Am. Mineral.* **88**, 830–836.

1210

1211 **Figure captions**

1212

1213 Figure 1. (a) Location of the 15° 20' N Fracture Zone, sampled by Ocean Drilling Program
1214 Leg 209, in the Atlantic Ocean. (b) Location of ODP Sites 1268a, 1272a, and 1274a. The
1215 location of the active Logatchev Hydrothermal Field is also shown. Bathymetry from
1216 Lagabrielle et al. (1998).

1217

1218 Figure 2. Downhole variation in metres below seafloor (mbsf) of primary lithology, intensity
1219 of alteration, loss on ignition (LOI) and SiO₂ wt. %. Modified after Bach et al. (2004) and
1220 Paulick et al. (2006).

1221

1222 Figure 3. The mineralogical control of Hole 1268a bulk-rock compositions. (a) Bulk-rock
1223 MgO/SiO₂ vs. Al₂O₃/SiO₂. Solid line is the "Terrestrial Array for peridotite" of Jagoutz et al.
1224 (1979). Hole 1272a and 1274a serpentinites from Harvey et al. (2006) and Godard et al.
1225 (2008). Large oval symbols denote Hole 1268a samples from this study, small round symbols
1226 denote equivalent Hole 1268a lithologies of Paulick et al. (2006). Talc- (± chlorite-) altered
1227 serpentinites are labelled according to the core section they were recovered from. (b) Mineral

1228 major element compositions of serpentine (lizardite), bastite pseudomorphs of orthopyroxene,
1229 chlorite and talc. Bulk-rock compositions in (a) are readily accounted for by simple mixing of
1230 mineralogical components in (b). Endmember mineral compositions from Yalçın and
1231 Bozkaya, (2006) (talc), Harvey et al. (2012) (opx and cpx), Padrón-Navarta et al. (2011)
1232 (chlorite). Large symbols = this study. Small symbols = Moll et al. (2007). * = analyses of
1233 talc after olivine from this study with reduced beam size (4-8 µm).

1234

1235 Figure 4. Strontium and boron isotope variation with depth at Hole 1268a. (a) $^{87}\text{Sr}/^{86}\text{Sr}$ versus
1236 depth (mbsf). Oval symbols as in Figure 3a. White squares are the leached residues of 2R2
1237 27-35 (A), 2R2 83-89 (B), 4R1 44-55 (C) and 6R1 100-110 (D). Leached samples are tied to
1238 their respective unleached sample by dotted lines. Hashed field denotes range of values
1239 reported by Vils et al. (2009). Light grey field denotes range of compositions obtained for
1240 serpentinites from Atlantis Massif (Boschi et al., 2008). Dark grey field denotes talc- and talc
1241 + chlorite-altered serpentinites from Atlantis Massif (Boschi et al., 2008). (b) Boron isotope
1242 variability with depth. Symbols and fields as in (a) above.

1243

1244 Figure 5. Boron and strontium abundances in Hole 1268a serpentinites and talc-altered
1245 serpentinites. Concentrations expressed in $\mu\text{g g}^{-1}$.

1246

1247 Figure 6. Fluid-mineral fractionation as a function of pH and temperature. (a) Relative
1248 speciation of boric acid versus borate as a function of pH at 25 °C (Hemming and Hanson,
1249 1992). Stippled area denotes possible range of seawater pH (after Boschi et al., 2008). Dark
1250 grey shading denotes pH conditions prevalent during Si-metasomatism / talc-alteration (Bach
1251 et al., 2004). Light grey shading denotes likely range of pH conditions experienced during the
1252 serpentinization of ODP Leg 209 serpentinites (Vils et al., 2009). (b) Despite the contraction

1253 of the possible magnitude of fluid-mineral fractionation with increasing temperature, under
1254 the conditions prevalent during Si-metasomatism, a fluid-mineral fractionation factor of for
1255 $\delta^{11}\text{B}$ of c. +19 ‰ is still possible, independent of any differences in initial fluid composition
1256 between the early serpentinizing fluid and the later talc-alteration-related fluid. Modified after
1257 Foustoukos et al., 2008; Boschi et al. (2008).

1258

1259 Figure 7. Strontium and boron isotope evolution diagram for Hole 1268a serpentinites. A
1260 melt-depleted peridotite precursor is progressively serpentinized at c. 200 °C (Process 1),
1261 resulting in a rapid increase in $\delta^{11}\text{B}$ and likely accompanied by an equally rapid increase in
1262 [B] (not illustrated). At relatively low fluid / rock ratios, i.e. when < 10% of the peridotite Sr
1263 budget has been exchanged with seawater, the serpentinite has already acquired a seawater-
1264 like $\delta^{11}\text{B}$. Continued fluid / rock interaction has little further effect upon $\delta^{11}\text{B}$ but continues to
1265 increase serpentinite $^{87}\text{Sr}/^{86}\text{Sr}$ by exchanging 75 to 100 % of the original mantle-like Sr.
1266 Subsequent interaction with a low-pH, high-T fluid (> 300 °C; Bach et al. 2004) and the
1267 consequent alteration to a talc-bearing lithology results in dehydration, loss of B and a shift to
1268 lighter $\delta^{11}\text{B}$ (Process 2; see text for details). The large grey arrow with solid outline denotes
1269 the shift in $\delta^{11}\text{B}$ possible starting from the most ^{11}B -rich of the precursor samples of Vils et
1270 al. (2009) whereas the large grey arrow with the dashed outline denotes range of possible
1271 $\delta^{11}\text{B}$ using the least ^{11}B -rich sample of Vils et al. (2009) as a precursor. Both arrows span a
1272 range of 19 ‰ – the possible range calculated in Figure 6b for these pH-temperature
1273 conditions. This differs from the inferred process of talc-alteration and acquisition of boron
1274 isotope signatures suggested by Boschi et al. (2008). Small numbers near narrow dashed,
1275 dotted and solid curves indicate modelled water / rock ratios. Figure modified after Boschi et
1276 al. (2008).

| Hole | Core | Section | Lithology | Interval - top | bottom | Piece no. | Depth (mbsf) |
|-------|------|---------|-----------|----------------|--------|-----------|--------------|
| 1268a | 2R | 2 | S | 27 | 35 | 4 | 15.19 |
| 1268a | 2R | 2 | S | 83 | 89 | 10 | 15.67 |
| 1268a | 4R | 1 | S | 44 | 55 | 9 | 25.24 |
| 1268a | 6R | 1 | S | 100 | 106 | 15 | 35.40 |
| 1268a | 8R | 1 | T | 28 | 35 | 8 | 44.28 |
| 1268a | 8R | 1 | T | 108 | 114 | 25 | 45.08 |
| 1268a | 8R | 2 | S | 14 | 20 | 3 | 45.64 |
| 1268a | 10R | 1 | S | 35 | 41 | 7 | 53.95 |
| 1268a | 11R | 1 | T | 39 | 45 | 8 | 58.99 |
| 1268a | 12R | 1 | S | 41 | 46 | 3 | 63.61 |
| 1268a | 13R | 1 | S | 46 | 55 | 6 | 68.66 |
| 1268a | 14R | 1 | T | 90 | 96 | 16 | 73.70 |
| 1268a | 15R | 3 | T | 38 | 44 | 1 | 80.78 |
| 1268a | 16R | 2 | T | 88 | 94 | 4 | 84.49 |
| 1268a | 18R | 3 | T | 87 | 93 | 9 | 95.59 |
| 1268a | 18R | 1 | T | 100 | 110 | 10 | 95.72 |
| 1268a | 19R | 1 | S | 34 | 44 | 1 | 97.34 |
| 1268a | 19R | 2 | S | 104 | 110 | 14 | 98.04 |
| 1268a | 19R | 4 | S | 61 | 67 | 1 | 101.41 |
| 1268a | 20R | 1 | S | 100 | 110 | 8 | 102.60 |
| 1268a | 23R | 3 | S | 92 | 98 | 4 | 119.83 |
| 1268a | 27R | 1 | G | 102 | 108 | 8 | 136.53 |
| 1268a | 29R | 1 | G | 123 | 129 | 14 | 146.33 |

Table 1. Samples from ODP Leg 209 Site 1268 used in this study. Site 1268 is located at 14°50.755 N, 45°04.641 W, and commenced at a water depth of 3007 m. The Hole penetrated to a depth of 146.7 metres below seafloor (mbsf) and 78.7 m of material was recovered, with primary lithologies comprising 63 % harzburgite, 11 % dunite and 26 % gabbro. Lithologies sampled were serpentinite (S), talc-altered serpentinite (T), and gabbro / micro-gabbro (G). Core images of the samples can be found at http://www-odp.tamu.edu/publications/209_ir/volume/cores/cor_1268.pdf.

| Sample | Lithology | | $^{87}\text{Sr}/^{86}\text{Sr}$ | 2 σ | [Sr] |
|--------------------|---------------------------|-----------------|---------------------------------|------------|-------|
| 1268a 2R2 27-35 | serpentinite | bulk rock | 0.71196 | 0.00015 | 2.44 |
| | | acetic leach | 0.71727 | 0.00088 | 13.00 |
| | | HCl leach | na | na | na |
| | | leached residue | 0.707630 | 0.000030 | 0.12 |
| 1268a 2R2 83-89 | serpentinite | bulk rock | 0.709012 | 0.000005 | 1.97 |
| | | acetic leach | 0.70912 | 0.00002 | 10.81 |
| | | HCl leach | 0.70918 | 0.00001 | 4.10 |
| | | leached residue | 0.70871 | 0.00007 | 0.37 |
| 1268a 4R1 44-55 | serpentinite | bulk rock | 0.708995 | 0.000009 | 2.01 |
| | | acetic leach | 0.70921 | 0.00001 | 8.51 |
| | | HCl leach | 0.70906 | 0.00002 | 2.03 |
| | | leached residue | 0.707668 | 0.000008 | 0.14 |
| 1268a 6R1 100-106 | serpentinite | bulk rock | 0.709004 | 0.000007 | 2.18 |
| | | acetic leach | 0.70916 | 0.00003 | 10.70 |
| | | HCl leach | 0.70901 | 0.00001 | 1.34 |
| | | leached residue | 0.70784 | 0.00005 | 0.14 |
| 1268a 8R1 28-35 | talc-altered serpentinite | bulk rock | 0.709102 | 0.000009 | na |
| 1268a 8R1 108-114 | talc-altered serpentinite | bulk rock | 0.708731 | 0.000009 | 2.38 |
| 1268a 8R2 14-20 | serpentinite | bulk rock | 0.70882 | 0.000009 | 1.02 |
| 1268a 10R1 35-41 | talc-altered serpentinite | bulk rock | 0.708912 | 0.000007 | 1.77 |
| 1268a 11R1 39-45 | talc-altered serpentinite | bulk rock | 0.709149 | 0.000006 | 0.41 |
| 1268a 12R1 41-46 | serpentinite | bulk rock | 0.708857 | 0.000006 | 1.43 |
| 1268a 13R1 46-55 | serpentinite | bulk rock | 0.708978 | 0.000008 | 1.03 |
| 1268a 14R1 90-96 | talc-altered serpentinite | bulk rock | 0.708928 | 0.000011 | 0.62 |
| 1268a 15R3 38-44 | talc-altered serpentinite | bulk rock | 0.708805 | 0.000005 | 1.03 |
| 1268a 16R2 88-94 | talc-altered serpentinite | bulk rock | 0.709093 | 0.000006 | 1.38 |
| 1268a 18R3 87-93 | talc-altered serpentinite | bulk rock | 0.707466 | 0.000050 | 2.23 |
| 1268a 18R3 100-110 | talc-altered serpentinite | bulk rock | 0.709054 | 0.000006 | 1.55 |
| 1268a 19R1 34-43 | serpentinite | bulk rock | 0.709236 | 0.000022 | 0.88 |
| 1268a 19R2 104-110 | talc-altered serpentinite | bulk rock | 0.707318 | 0.000006 | 1.69 |
| 1268a 19R4 61-67 | serpentinite | bulk rock | 0.708416 | 0.000007 | 0.95 |
| 1268a 20R1 100-110 | serpentinite | bulk rock | 0.709054 | 0.000008 | 1.16 |
| 1268a 23R3 92-98 | serpentinite | bulk rock | 0.709110 | 0.000010 | 1.13 |
| 1268a 27R1 102-108 | (micro) gabbro-norite | bulk rock | 0.70294 | 0.000009 | 72.8 |
| 1268a 29R1 123-129 | (micro) gabbro-norite | bulk rock | 0.703094 | 0.000011 | 86.9 |

Table 2. Strontium isotope and abundance analyses of ODP Leg 209 Hole 1268a serpentinites, talc-altered serpentinites and gabbro. Instrumental mass fractionation corrected for by normalizing results to $^{86}\text{Sr}/^{88}\text{Sr} = 0.1194$ for isotope measurements. Sr blank was negligible compared to the amount of material processed (typically several hundred ng Sr). SRM 987 reference material (n = 11) during the course of the measurements gave an average $^{87}\text{Sr}/^{86}\text{Sr} = 0.710248 \pm 4$. 2R2 27-35, 2R2 87-93, 4R1 44-55 and 6R1 100-106 were sequentially leached (10 % glacial acetic acid then, 1.5M Romil UpA HCl). Strontium abundance expressed in $\mu\text{g g}^{-1}$.

| Sample | Lithology | $^{11}\text{B}/^{10}\text{B}$ | $\delta^{11}\text{B}$ | 2σ | [B] |
|--------------------|-------------------------|-------------------------------|-----------------------|-----------|-----|
| 1268A 2R2 27-35 | serpentine | 4.1004 | 11.60 | 0.32 | 29 |
| 1268A 2R2 83-89 | serpentine | 4.1080 | 15.93 | 0.24 | 36 |
| 1268A 4R1 44-55 | serpentine | 4.0951 | 10.29 | 0.25 | 28 |
| 1268A 6R1 100-106 | serpentine | 4.0847 | 10.16 | 0.37 | 26 |
| 1268A 8R1 28-35 | talc-altered serpentine | na | na | na | na |
| 1268A 8R1 108-114 | talc-altered serpentine | 4.0981 | 13.47 | 0.74 | 12 |
| 1268A 8R2 14-20 | serpentine | na | na | na | na |
| 1268A 10R1 35-41 | talc-altered serpentine | 4.087 | 10.73 | 2.97 | <3 |
| 1268A 11R1 39-45 | talc-altered serpentine | na | na | na | na |
| 1268A 12R1 41-46 | serpentine | 4.0946 | 12.60 | 0.19 | 20 |
| 1268A 13R1 46-55 | serpentine | 4.0909 | 9.25 | 0.35 | 24 |
| 1268A 14R1 90-96 | talc-altered serpentine | na | na | na | na |
| 1268A 15R3 38-44 | talc-altered serpentine | 4.1171 | 18.17 | 0.40 | 4 |
| 1268A 16R2 88-94 | talc-altered serpentine | 4.094 | 12.5 | 3.7 | 5 |
| 1268A 18R3 87-93 | talc-altered serpentine | 4.0927 | 12.1 | 2.3 | 5 |
| 1268A 18R3 100-110 | talc-altered serpentine | 4.0925 | 9.65 | 0.99 | <3 |
| 1268A 19R1 34-43 | serpentine | na | na | na | na |
| 1268A 19R2 104-110 | talc-altered serpentine | na | na | na | na |
| 1268A 19R4 61-67 | serpentine | 4.1227 | 19.56 | 0.32 | 20 |
| 1268A 20R1 100-110 | serpentine | 4.1218 | 16.87 | 0.30 | 27 |
| 1268A 23R3 92-98 | serpentine | 4.1157 | 17.83 | 0.37 | 19 |

Table 3. Boron isotope analyses of ODP Leg 209 Hole 1268a serpentinites, talc-altered serpentinites. $^{11}\text{B}/^{10}\text{B}$ isotopic ratio is reported in standard delta notation as permil (‰) deviation from the mean value for the SRM-951 boric acid standard. Boron abundances ([B]) expressed in $\mu\text{g g}^{-1}$.

Table(s)

| Sample | SiO ₂ | TiO ₂ | Al ₂ O ₃ | Fe ₂ O ₃ | MnO | MgO | CaO | Na ₂ O | K ₂ O | P ₂ O ₅ | SO ₃ | Cr ₂ O ₃ | NiO | LOI | Total |
|---------------------|------------------|------------------|--------------------------------|--------------------------------|-------|------|------|-------------------|------------------|-------------------------------|-----------------|--------------------------------|-------|------|-------|
| 1268a 2R2 27-35 | 41.3 | 0.018 | 0.60 | 8.35 | 0.061 | 37.2 | bdl | bdl | 0.002 | bdl | 0.327 | 0.342 | 0.290 | 11.3 | 99.8 |
| 1268a 2R2 27-35* | 41.5 | 0.019 | 0.62 | 8.08 | 0.057 | 37.1 | 0.03 | 0.11 | 0.013 | 0.011 | na | na | na | 11.8 | 99.3 |
| 1268a 2R2 83-89 | 40.0 | 0.018 | 0.64 | 7.88 | 0.092 | 38.6 | bdl | bdl | bdl | bdl | 0.157 | 0.388 | 0.272 | 11.8 | 99.9 |
| 1268a 4R1 44-55 | 42.8 | 0.006 | 0.29 | 6.63 | 0.056 | 37.4 | bdl | bdl | 0.002 | bdl | 0.640 | 0.239 | 0.291 | 12.3 | 100.7 |
| 1268a 4R1 44-55* | 41.6 | 0.007 | 0.38 | 6.37 | 0.056 | 36.6 | 0.03 | 0.11 | 0.015 | 0.007 | na | na | na | 12.7 | 97.9 |
| 1268a 6R1 100-106 | 41.6 | 0.005 | 0.36 | 6.62 | 0.039 | 38.0 | 0.00 | bdl | 0.002 | bdl | 0.174 | 0.255 | 0.276 | 12.5 | 99.9 |
| 1268a 8R1 28-35* | 59.3 | 0.016 | 0.90 | 5.69 | 0.085 | 28.1 | 0.10 | 0.24 | 0.019 | 0.008 | na | na | na | 4.4 | 98.7 |
| 1268a 8R1 108-114 | 56.8 | 0.105 | 0.88 | 7.08 | 0.074 | 28.5 | 0.18 | 0.20 | 0.010 | 0.024 | 0.075 | 0.259 | 0.245 | 5.4 | 99.8 |
| 1268a 8R2 14-20 | 43.5 | 0.006 | 0.45 | 6.42 | 0.108 | 37.3 | 0.01 | bdl | bdl | bdl | 0.137 | 0.285 | 0.284 | 11.3 | 99.8 |
| 1268a 10R1 35-41 | 29.7 | 0.350 | 19.7 | 14.4 | 0.383 | 24.5 | 0.01 | 0.13 | 0.009 | bdl | bdl | 0.083 | 0.036 | 10.5 | 99.8 |
| 1268a 11R1 39-45 | 59.1 | 0.006 | 0.16 | 5.61 | 0.062 | 29.1 | bdl | 0.02 | bdl | bdl | 0.258 | 0.158 | 0.201 | 5.1 | 99.9 |
| 1268a 12R1 41-46 | 40.8 | 0.121 | 0.89 | 8.25 | 0.122 | 36.5 | bdl | 0.01 | 0.002 | bdl | 0.162 | 0.331 | 0.267 | 12.0 | 99.4 |
| 1268a 13R1 46-55 | 42.5 | 0.005 | 0.42 | 6.90 | 0.060 | 37.6 | bdl | bdl | bdl | bdl | 0.155 | 0.302 | 0.281 | 11.7 | 100.0 |
| 1268a 14R1 90-96 | 60.9 | 0.019 | 0.25 | 6.21 | 0.095 | 28.3 | bdl | 0.01 | bdl | bdl | 0.007 | 0.056 | 0.240 | 4.4 | 100.5 |
| 1268a 15R3 38-44 | 56.6 | 0.005 | 0.30 | 5.12 | 0.093 | 31.0 | bdl | bdl | bdl | bdl | 0.124 | 0.151 | 0.220 | 6.0 | 99.6 |
| 1268a 16R2 88-94 | 59.7 | 0.006 | 0.66 | 5.07 | 0.059 | 29.1 | 0.00 | 0.10 | bdl | bdl | 0.047 | 0.174 | 0.230 | 4.9 | 100.1 |
| 1268a 18R1 100-110* | 64.1 | 0.028 | 0.76 | 4.55 | 0.062 | 31.4 | 0.05 | 0.19 | 0.015 | 0.011 | na | na | na | 5.4 | 106.5 |
| 1268a 18R3 87-93 | 42.5 | 0.202 | 9.83 | 7.99 | 0.272 | 29.1 | 1.47 | 0.12 | 0.011 | 0.003 | bdl | 0.013 | 0.026 | 8.4 | 99.9 |
| 1268a 19R1 34-43 | 39.9 | 0.008 | 0.43 | 7.53 | 0.071 | 38.5 | bdl | bdl | bdl | bdl | 0.247 | 0.324 | 0.276 | 12.1 | 99.4 |
| 1268a 19R1 34-43* | 40.4 | 0.011 | 0.44 | 7.55 | 0.070 | 38.8 | 0.03 | 0.08 | 0.012 | 0.005 | na | na | na | 12.6 | 100.1 |
| 1268a 19R2 104-110 | 33.7 | 0.878 | 14.2 | 12.4 | 0.502 | 27.3 | 1.02 | 0.06 | bdl | bdl | 0.029 | 0.019 | 0.020 | 10.0 | 100.0 |
| 1268a 19R4 61-67 | 39.9 | 0.006 | 0.66 | 7.57 | 0.063 | 38.8 | bdl | bdl | bdl | bdl | 0.246 | 0.577 | 0.287 | 11.8 | 99.9 |
| 1268a 20R1 100-110 | 40.6 | 0.005 | 0.63 | 7.02 | 0.071 | 38.8 | bdl | 0.02 | bdl | bdl | 0.178 | 0.479 | 0.265 | 12.0 | 100.1 |
| 1268a 20R1 100-110* | 40.9 | 0.008 | 0.64 | 6.88 | 0.070 | 38.8 | 0.04 | 0.14 | 0.013 | 0.009 | na | na | na | 12.7 | 100.2 |
| 1268a 23R3 92-98 | 41.7 | 0.010 | 0.51 | 7.19 | 0.066 | 38.5 | 0.01 | bdl | bdl | bdl | 0.047 | 0.281 | 0.283 | 11.9 | 100.5 |
| 1268a 27R2 102-108 | 49.5 | 0.239 | 17.8 | 6.32 | 0.146 | 9.49 | 13.1 | 2.12 | 0.032 | bdl | bdl | 0.001 | 0.009 | 1.7 | 100.5 |
| 1268a 29R1 123-129 | 47.2 | 0.291 | 15.2 | 8.19 | 0.181 | 12.6 | 11.9 | 1.73 | 0.030 | bdl | bdl | 0.003 | 0.011 | 2.7 | 100.1 |

Table S1. Whole rock major element abundances expressed as weight percent (wt. %). (*) Denotes XRF measurement made at The Open University, all others performed by XRF at the University of Leicester. Major element and Ni data quality was assessed using two WS-E and OUG-94 at The Open University and a suite of ultramafic reference materials (including UM-1, UM-2, UM-4, JP-1 and PCC-1) at the University of Leicester. Reproducibility of reference materials is within 2% of recommended values and in excellent agreement between the two laboratories. LOI = loss on ignition. bdl = below detection limit. na = not analysed.

Table(s)

| | SiO ₂ | TiO ₂ | Al ₂ O ₃ | Cr ₂ O ₃ | FeO | MnO | MgO | CaO | NiO | Na ₂ O | K ₂ O |
|-----------------------------|------------------|------------------|--------------------------------|--------------------------------|-------|-------|-------|-------|-------|-------------------|------------------|
| 10R1 35-41 chlorite spot 1 | 35.35 | 0.016 | 20.16 | 0.098 | 15.29 | 0.742 | 28.07 | 0.163 | 0.093 | 0.024 | 0.006 |
| 10R1 35-41 chlorite spot 2 | 35.96 | 0.001 | 19.47 | 0.094 | 15.88 | 0.828 | 27.54 | 0.140 | 0.053 | 0.017 | 0.007 |
| 10R1 35-41 chlorite spot 3 | 35.13 | 0.034 | 19.34 | 0.082 | 17.02 | 0.847 | 27.34 | 0.112 | 0.071 | 0.013 | 0.012 |
| 10R1 35-41 chlorite spot 4 | 35.51 | 0.030 | 19.41 | 0.161 | 16.34 | 0.839 | 27.43 | 0.124 | 0.117 | 0.033 | 0.010 |
| 10R1 35-41 chlorite spot 5 | 35.24 | 0.015 | 19.57 | 0.107 | 16.98 | 0.922 | 26.92 | 0.109 | 0.112 | 0.000 | 0.013 |
| 10R1 35-41 chlorite spot 6 | 35.61 | 0.018 | 18.99 | 0.088 | 16.74 | 0.899 | 27.48 | 0.116 | 0.037 | 0.023 | 0.005 |
| 10R1 35-41 chlorite spot 7 | 35.60 | 0.007 | 20.11 | 0.113 | 15.59 | 0.808 | 27.52 | 0.145 | 0.060 | 0.047 | 0.000 |
| 10R1 35-41 chlorite spot 8 | 35.51 | 0.009 | 19.93 | 0.350 | 15.76 | 0.874 | 27.24 | 0.153 | 0.081 | 0.075 | 0.019 |
| 10R1 35-41 chlorite spot 9 | 35.59 | 0.013 | 20.23 | 0.091 | 15.34 | 0.842 | 27.62 | 0.147 | 0.063 | 0.046 | 0.010 |
| 10R1 35-41 chlorite spot 10 | 35.55 | 0.000 | 19.65 | 0.097 | 16.44 | 0.926 | 27.17 | 0.136 | 0.000 | 0.025 | 0.009 |
| 10R1 35-41 chlorite spot 11 | 35.58 | 0.012 | 20.34 | 0.087 | 15.19 | 0.863 | 27.71 | 0.130 | 0.048 | 0.027 | 0.003 |
| 10R1 35-41 chlorite spot 12 | 34.65 | 0.014 | 21.89 | 0.047 | 14.34 | 0.656 | 28.20 | 0.134 | 0.041 | 0.020 | 0.003 |
| 10R1 35-41 chlorite spot 13 | 34.78 | 0.000 | 21.67 | 0.051 | 14.30 | 0.685 | 28.29 | 0.119 | 0.079 | 0.022 | 0.000 |
| 10R1 35-41 chlorite spot 14 | 35.26 | 0.042 | 21.50 | 0.064 | 14.20 | 0.623 | 28.09 | 0.156 | 0.030 | 0.030 | 0.005 |
| 10R1 35-41 chlorite spot 15 | 35.56 | 0.026 | 20.89 | 0.112 | 14.46 | 0.655 | 28.08 | 0.118 | 0.062 | 0.025 | 0.009 |
| 10R1 35-41 chlorite spot 16 | 35.10 | 0.002 | 21.11 | 0.093 | 14.60 | 0.682 | 28.20 | 0.139 | 0.068 | 0.000 | 0.008 |
| 10R1 35-41 chlorite spot 17 | 35.24 | 0.053 | 21.05 | 0.109 | 14.54 | 0.657 | 28.16 | 0.137 | 0.029 | 0.004 | 0.014 |
| 10R1 35-41 chlorite spot 18 | 35.03 | 0.022 | 22.68 | 0.255 | 12.44 | 0.334 | 28.98 | 0.147 | 0.056 | 0.061 | 0.000 |
| 10R1 35-41 chlorite spot 19 | 35.67 | 0.020 | 22.97 | 0.130 | 11.90 | 0.163 | 28.96 | 0.122 | 0.056 | 0.016 | 0.001 |
| 10R1 35-41 chlorite spot 20 | 34.88 | 0.018 | 21.50 | 0.247 | 13.61 | 0.666 | 28.88 | 0.085 | 0.079 | 0.037 | 0.004 |
| 10R1 35-41 chlorite spot 21 | 35.39 | 0.012 | 21.90 | 0.173 | 12.70 | 0.475 | 29.13 | 0.083 | 0.086 | 0.047 | 0.010 |
| 10R1 35-41 chlorite spot 22 | 34.88 | 0.004 | 21.09 | 0.228 | 14.25 | 0.847 | 28.49 | 0.097 | 0.078 | 0.029 | 0.013 |
| 10R1 35-41 chlorite spot 23 | 34.01 | 0.010 | 21.49 | 0.128 | 12.23 | 0.310 | 31.48 | 0.211 | 0.077 | 0.055 | 0.000 |
| 10R1 35-41 chlorite spot 24 | 35.32 | 0.020 | 23.24 | 0.017 | 12.47 | 0.271 | 28.34 | 0.156 | 0.074 | 0.061 | 0.026 |
| 10R1 35-41 chlorite spot 25 | 36.14 | 0.021 | 21.68 | 0.067 | 12.08 | 0.192 | 29.64 | 0.128 | 0.041 | 0.000 | 0.000 |
| 10R1 35-41 chlorite spot 26 | 35.43 | 0.000 | 21.69 | 0.253 | 12.38 | 0.403 | 29.70 | 0.128 | 0.000 | 0.008 | 0.002 |
| 10R1 35-41 chlorite spot 27 | 34.70 | 0.000 | 24.13 | 0.000 | 11.77 | 0.204 | 28.83 | 0.307 | 0.026 | 0.029 | 0.001 |

Table S2.1. Electron microprobe analyses of chlorite from sample 10R1 35-41, Hole 1268a. Analyses normalized to anhydrous composition. Operating conditions: Accelerating voltage of 15 kV, beam current 15nA, beam size 10 μm .

| | SiO ₂ | TiO ₂ | Al ₂ O ₃ | Cr ₂ O ₃ | FeO | MnO | MgO | CaO | NiO | Na ₂ O | K ₂ O |
|----------------------|------------------|------------------|--------------------------------|--------------------------------|-------|-------|-------|-------|-------|-------------------|------------------|
| Serpentine after opx | | | | | | | | | | | |
| 6R1 100-106 spot 1 | 47.04 | 0.009 | 2.87 | 0.854 | 5.56 | 0.067 | 43.35 | 0.062 | 0.118 | 0.046 | 0.024 |
| 6R1 100-106 spot 2 | 47.63 | 0.023 | 2.25 | 1.331 | 7.67 | 0.096 | 40.66 | 0.129 | 0.133 | 0.044 | 0.025 |
| 6R1 100-106 spot 3 | 46.99 | 0.036 | 3.34 | 1.062 | 5.65 | 0.063 | 42.65 | 0.068 | 0.070 | 0.053 | 0.020 |
| 6R1 100-106 spot 4 | 47.85 | 0.020 | 1.93 | 1.441 | 7.69 | 0.103 | 40.59 | 0.035 | 0.151 | 0.114 | 0.076 |
| 6R1 100-106 spot 5 | 47.32 | 0.008 | 2.28 | 1.361 | 7.89 | 0.085 | 40.64 | 0.136 | 0.180 | 0.078 | 0.023 |
| 6R1 100-106 spot 6 | 47.01 | 0.028 | 1.57 | 0.979 | 9.12 | 0.099 | 40.92 | 0.081 | 0.128 | 0.055 | 0.003 |
| 6R1 100-106 spot 7 | 47.32 | 0.043 | 1.85 | 1.095 | 11.25 | 0.135 | 37.99 | 0.094 | 0.182 | 0.023 | 0.020 |
| 6R1 100-106 spot 8 | 47.02 | 0.000 | 1.88 | 1.038 | 11.83 | 0.124 | 37.77 | 0.120 | 0.169 | 0.019 | 0.028 |
| 6R1 100-106 spot 9 | 48.24 | 0.012 | 1.29 | 0.408 | 10.29 | 0.091 | 39.39 | 0.088 | 0.159 | 0.013 | 0.015 |
| 6R1 100-106 spot 10 | 47.25 | 0.026 | 1.70 | 0.899 | 11.22 | 0.156 | 38.37 | 0.149 | 0.121 | 0.069 | 0.042 |
| 6R1 100-106 spot 11 | 47.13 | 0.014 | 1.81 | 0.920 | 11.46 | 0.118 | 38.22 | 0.062 | 0.180 | 0.058 | 0.025 |
| 6R1 100-106 spot 12 | 46.87 | 0.006 | 1.95 | 1.006 | 11.40 | 0.051 | 38.48 | 0.077 | 0.105 | 0.035 | 0.033 |
| 6R1 100-106 spot 13 | 47.37 | 0.001 | 1.68 | 0.737 | 11.86 | 0.090 | 37.93 | 0.096 | 0.165 | 0.050 | 0.021 |
| 6R1 100-106 spot 14 | 47.39 | 0.000 | 1.70 | 0.773 | 11.57 | 0.141 | 38.08 | 0.074 | 0.210 | 0.033 | 0.027 |

| | SiO ₂ | TiO ₂ | Al ₂ O ₃ | Cr ₂ O ₃ | FeO | MnO | MgO | CaO | NiO | Na ₂ O | K ₂ O |
|--------------------------|------------------|------------------|--------------------------------|--------------------------------|------|-------|-------|-------|-------|-------------------|------------------|
| Serpentine after olivine | | | | | | | | | | | |
| 6R1 100-106 spot 1 | 49.11 | 0.012 | 0.45 | 0.000 | 4.82 | 0.059 | 45.17 | 0.045 | 0.283 | 0.043 | 0.006 |
| 6R1 100-106 spot 2 | 49.17 | 0.000 | 0.37 | 0.016 | 4.41 | 0.033 | 45.72 | 0.031 | 0.218 | 0.020 | 0.010 |
| 6R1 100-106 spot 3 | 49.72 | 0.000 | 0.20 | 0.000 | 3.70 | 0.040 | 46.15 | 0.000 | 0.175 | 0.014 | 0.004 |
| 6R1 100-106 spot 4 | 49.75 | 0.003 | 0.31 | 0.000 | 3.93 | 0.036 | 45.69 | 0.033 | 0.257 | 0.002 | 0.000 |
| 6R1 100-106 spot 5 | 50.13 | 0.001 | 0.22 | 0.015 | 3.73 | 0.045 | 45.68 | 0.016 | 0.139 | 0.016 | 0.009 |
| 6R1 100-106 spot 6 | 49.03 | 0.017 | 0.25 | 0.013 | 4.90 | 0.021 | 45.33 | 0.038 | 0.343 | 0.042 | 0.011 |
| 6R1 100-106 spot 7 | 49.60 | 0.000 | 0.22 | 0.000 | 4.14 | 0.004 | 45.64 | 0.028 | 0.328 | 0.027 | 0.008 |
| 6R1 100-106 spot 8 | 49.44 | 0.009 | 0.23 | 0.002 | 4.48 | 0.040 | 45.43 | 0.036 | 0.318 | 0.000 | 0.006 |
| 6R1 100-106 spot 9 | 49.59 | 0.006 | 0.38 | 0.000 | 4.68 | 0.037 | 44.81 | 0.083 | 0.398 | 0.011 | 0.014 |
| 6R1 100-106 spot 10 | 49.56 | 0.013 | 0.42 | 0.000 | 4.24 | 0.037 | 45.39 | 0.075 | 0.242 | 0.021 | 0.003 |
| 6R1 100-106 spot 11 | 49.37 | 0.011 | 0.35 | 0.004 | 4.39 | 0.041 | 45.35 | 0.061 | 0.419 | 0.000 | 0.007 |

| | | | | | | | | | | | |
|---------------------|-------|-------|------|-------|------|-------|-------|-------|-------|-------|-------|
| 6R1 100-106 spot 12 | 49.74 | 0.014 | 0.41 | 0.000 | 4.24 | 0.030 | 45.18 | 0.057 | 0.293 | 0.015 | 0.013 |
| 6R1 100-106 spot 13 | 49.05 | 0.000 | 0.39 | 0.042 | 4.58 | 0.064 | 45.54 | 0.047 | 0.252 | 0.014 | 0.021 |
| 6R1 100-106 spot 14 | 49.58 | 0.015 | 0.24 | 0.001 | 3.55 | 0.022 | 46.18 | 0.038 | 0.335 | 0.047 | 0.000 |
| 6R1 100-106 spot 15 | 49.90 | 0.000 | 0.27 | 0.022 | 3.17 | 0.038 | 46.14 | 0.046 | 0.336 | 0.058 | 0.019 |
| 6R1 100-106 spot 16 | 49.99 | 0.000 | 0.33 | 0.009 | 2.92 | 0.034 | 46.37 | 0.027 | 0.304 | 0.005 | 0.019 |

Table S2.2. Electron microprobe analyses of serpentine after orthopyroxene (opx) and serpentine after olivine from sample 6R1 100-106, Hole 1268a, ODP Leg 209. Composition normalized to anhydrous composition. Analytical conditions as Table S2.1.

| | SiO ₂ | TiO ₂ | Al ₂ O ₃ | Cr ₂ O ₃ | FeO | MnO | MgO | CaO | NiO | Na ₂ O | K ₂ O |
|-----------------------------|------------------|------------------|--------------------------------|--------------------------------|------|-------|-------|-------|-------|-------------------|------------------|
| <u>10 µm beam diameter</u> | | | | | | | | | | | |
| 6R1 100-106 talc spot 1 | 62.62 | 0.01 | 0.317 | 0.028 | 5.69 | 0.036 | 31.16 | 0.009 | 0.073 | 0.04 | 0.013 |
| 6R1 100-106 talc spot 2 | 55.99 | 0.004 | 0.302 | 0 | 5.37 | 0.026 | 38.04 | 0.022 | 0.222 | 0.024 | 0.009 |
| 6R1 100-106 talc spot 3 | 49.68 | 0.005 | 0.61 | 0.03 | 4.23 | 0.042 | 45.05 | 0.063 | 0.258 | 0.024 | 0.011 |
| 6R1 100-106 talc spot 4 | 63.27 | 0.001 | 0.25 | 0.008 | 6.07 | 0.046 | 30.2 | 0.015 | 0.105 | 0.043 | 0 |
| 6R1 100-106 talc spot 5 | 54.02 | 0 | 0.347 | 0 | 5.35 | 0.014 | 39.85 | 0.05 | 0.363 | 0 | 0.009 |
| 6R1 100-106 talc spot 6 | 49.65 | 0 | 0.461 | 0.02 | 3.19 | 0.006 | 46.39 | 0.042 | 0.195 | 0.021 | 0.02 |
| 6R1 100-106 talc spot 7 | 50.1 | 0 | 0.559 | 0.023 | 3.93 | 0.035 | 45.08 | 0.008 | 0.214 | 0.03 | 0.015 |
| 6R1 100-106 talc spot 8 | 51.44 | 0 | 0.638 | 0.006 | 4.42 | 0.045 | 43.12 | 0.158 | 0.147 | 0.017 | 0.011 |
| 6R1 100-106 talc spot 9 | 49.88 | 0.012 | 0.405 | 0 | 4.38 | 0.045 | 45.01 | 0.072 | 0.164 | 0.015 | 0.008 |
| 6R1 100-106 talc spot 10 | 62.88 | 0.007 | 0.462 | 0.012 | 6.9 | 0.051 | 29.52 | 0.014 | 0.066 | 0.082 | 0 |
| 6R1 100-106 talc spot 11 | 49.46 | 0.017 | 0.299 | 0.005 | 3.7 | 0.048 | 45.4 | 0.721 | 0.325 | 0.018 | 0.001 |
| 6R1 100-106 talc spot 12 | 63.99 | 0 | 0.418 | 0.006 | 6.36 | 0.02 | 29.09 | 0.017 | 0.043 | 0.047 | 0.01 |
| 6R1 100-106 talc spot 13 | 64.4 | 0.001 | 0.244 | 0 | 6.73 | 0.048 | 28.46 | 0.022 | 0.043 | 0.051 | 0.004 |
| 6R1 100-106 talc spot 14 | 49.45 | 0.017 | 0.483 | 0.003 | 4.36 | 0.033 | 45.32 | 0.091 | 0.218 | 0.013 | 0.013 |
| 6R1 100-106 talc spot 15 | 61.81 | 0.003 | 0.299 | 0.014 | 6.06 | 0.077 | 31.61 | 0.005 | 0.082 | 0.028 | 0.014 |
| 6R1 100-106 talc spot 16 | 51.08 | 0.002 | 0.462 | 0 | 3.68 | 0.046 | 44.51 | 0.038 | 0.165 | 0.021 | 0.003 |
| 6R1 100-106 talc spot 17 | 49.54 | 0.02 | 0.294 | 0 | 5.72 | 0.067 | 43.96 | 0.038 | 0.302 | 0.045 | 0.006 |
| 6R1 100-106 talc spot 18 | 52.28 | 0.028 | 0.56 | 0 | 4.57 | 0.074 | 42.22 | 0.029 | 0.181 | 0.041 | 0.013 |
| <u>4-6 µm beam diameter</u> | | | | | | | | | | | |
| 6R1 100-106 talc spot 1 | 64.39 | 0.01 | 0.15 | 0.02 | 6.86 | 0.05 | 28.36 | 0.02 | 0.05 | 0.05 | 0.02 |
| 6R1 100-106 talc spot 2 | 64.24 | 0 | 0.12 | 0 | 6.65 | 0.03 | 28.94 | 0 | 0.00 | 0.01 | 0 |
| 6R1 100-106 talc spot 3 | 64.20 | 0.02 | 0.15 | 0 | 6.74 | 0.06 | 28.69 | 0.01 | 0.09 | 0.01 | 0 |
| 6R1 100-106 talc spot 4 | 63.52 | 0 | 0.21 | 0.04 | 7.86 | 0.05 | 28.23 | 0.01 | 0 | 0.06 | 0.01 |

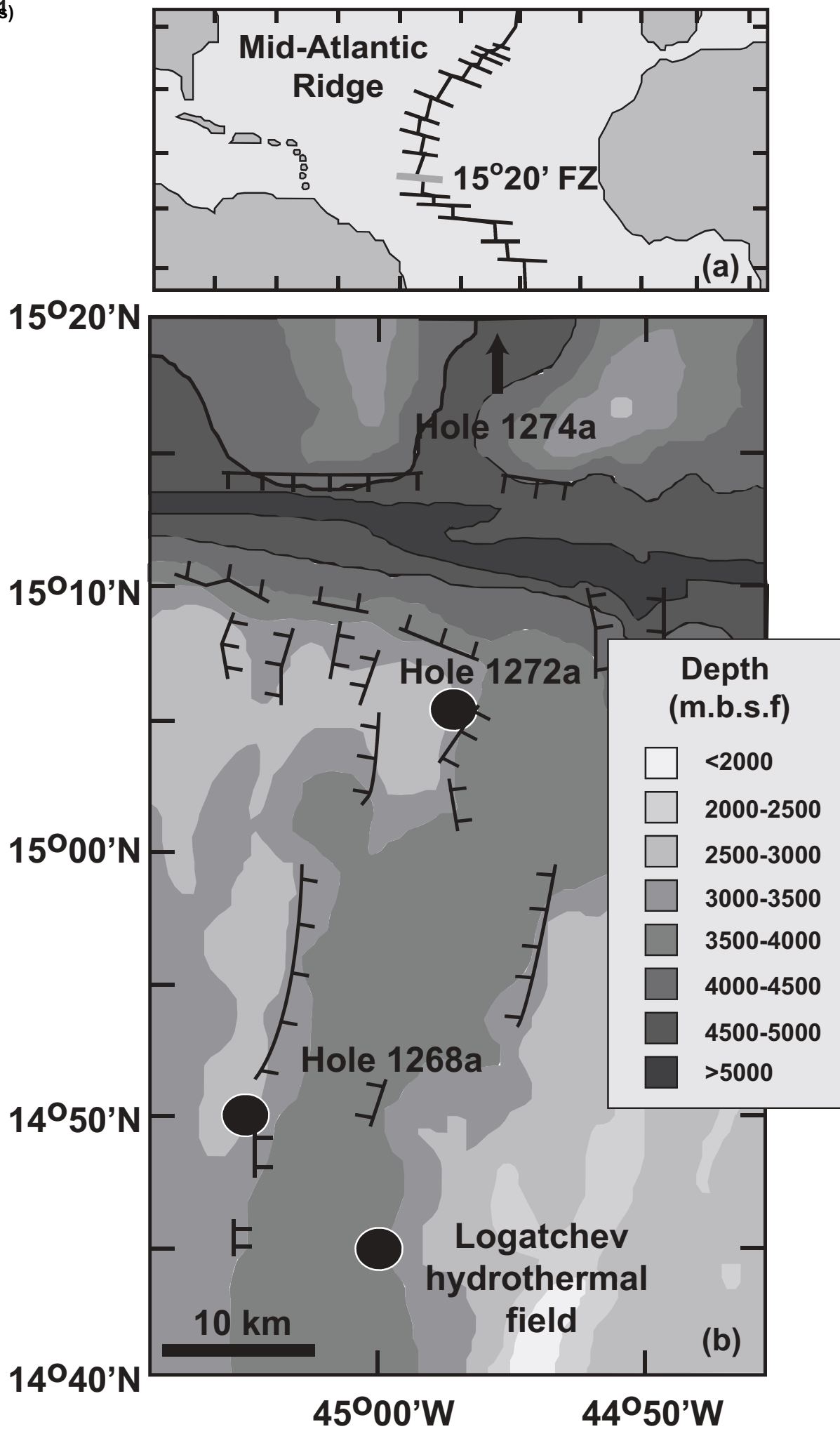
| | | | | | | | | | | | |
|-------------------------|-------|------|------|------|------|------|-------|------|------|------|------|
| 6R1 100-106 talc spot 5 | 64.02 | 0 | 0.20 | 0.01 | 7.74 | 0.03 | 27.87 | 0.01 | 0.06 | 0.03 | 0.02 |
| 6R1 100-106 talc spot 6 | 64.44 | 0 | 0.18 | 0 | 6.37 | 0.05 | 28.86 | 0 | 0 | 0.07 | 0.01 |
| 6R1 100-106 talc spot 7 | 63.45 | 0.01 | 0.15 | 0 | 7.24 | 0.05 | 28.98 | 0.01 | 0.03 | 0.06 | 0.01 |
| 6R1 100-106 talc spot 8 | 63.51 | 0 | 0.21 | 0 | 7.74 | 0.05 | 28.38 | 0 | 0.03 | 0.05 | 0.02 |
| 6R1 100-106 talc spot 9 | 62.91 | 0 | 0.19 | 0 | 7.57 | 0.04 | 29.22 | 0.02 | 0 | 0.01 | 0.03 |

Table S2.3. Electron microprobe analyses of talc from sample 6R1 100-106, Hole 1268a, ODP Leg 209. Composition normalized to anhydrous composition. Analytical conditions as Table S2.1.

| Sample | Original mass (g) | After leach (g) | Leached (g) | % leached |
|-----------------------------|---------------------------------|-----------------|-------------|-----------|
| 2R2 27-35 unleached | 0.0301 | 0.0260 | -0.0260 | 13.6 |
| 2R2 83-89 unleached | 0.0358 | 0.0326 | -0.0326 | 8.9 |
| 4R1 44-55 unleached | 0.0282 | 0.0228 | -0.0228 | 19.1 |
| 6R1 100-106 unleached | 0.0302 | 0.0252 | -0.0252 | 16.6 |
| | $^{87}\text{Sr}/^{86}\text{Sr}$ | +/- | [Sr] ppm | |
| 2R2 27-35 unleached | 0.711957 | 0.000152 | 2.44 | |
| 2R2 83-89 unleached | 0.709012 | 0.000005 | 1.97 | |
| 4R1 44-55 unleached | | | 2.01 | |
| 6R1 100-106 unleached | 0.709004 | 0.000007 | 2.18 | |
| 2R2 27-35 leached residue | 0.707627 | 0.000032 | 0.12 | |
| 2R2 83-89 leached residue | 0.708710 | 0.000062 | 0.37 | |
| 4R1 44-55 leached residue | 0.707656 | 0.000058 | 0.14 | |
| 6R1 100-106 leached residue | 0.707842 | 0.000037 | 0.14 | |
| 2R2 27-35 acetic leach | 0.717274 | 0.000843 | 13.003 | |
| 2R2 83-89 acetic leach | 0.709125 | 0.000017 | 10.81 | |
| 4R1 44-55 acetic leach | 0.709212 | 0.000012 | 8.51 | |
| 6R1 100-106 acetic leach | 0.709161 | 0.000026 | 10.72 | |
| 2R2 27-35 HCl leach | lost sample during drying | | | |
| 2R2 83-89 HCl leach | 0.709181 | 0.000006 | 4.10 | |
| 4R1 44-55 HCl leach | 0.709063 | 0.000014 | 2.03 | |
| 6R1 100-106 HCl leach | 0.709013 | 0.000001 | 1.34 | |

Table S3. Leaching experiments for uppermost samples recovered from Hole 1268a. First leach: 10 % glacial acetic acid for 15 minutes. Second leach 1.5M UpA HCl, for 15 minutes.

Figure 1)



Figure(s)

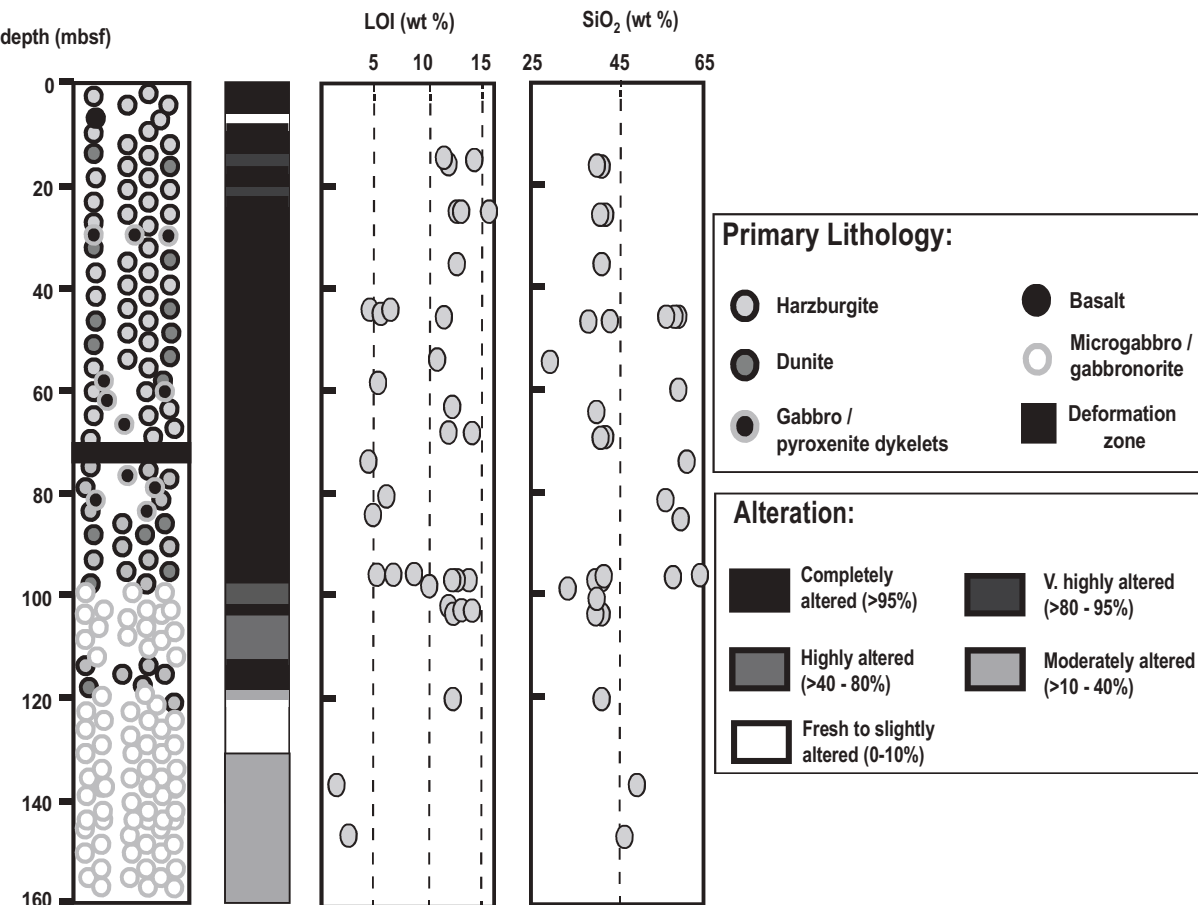


Figure 2

Figure(s)

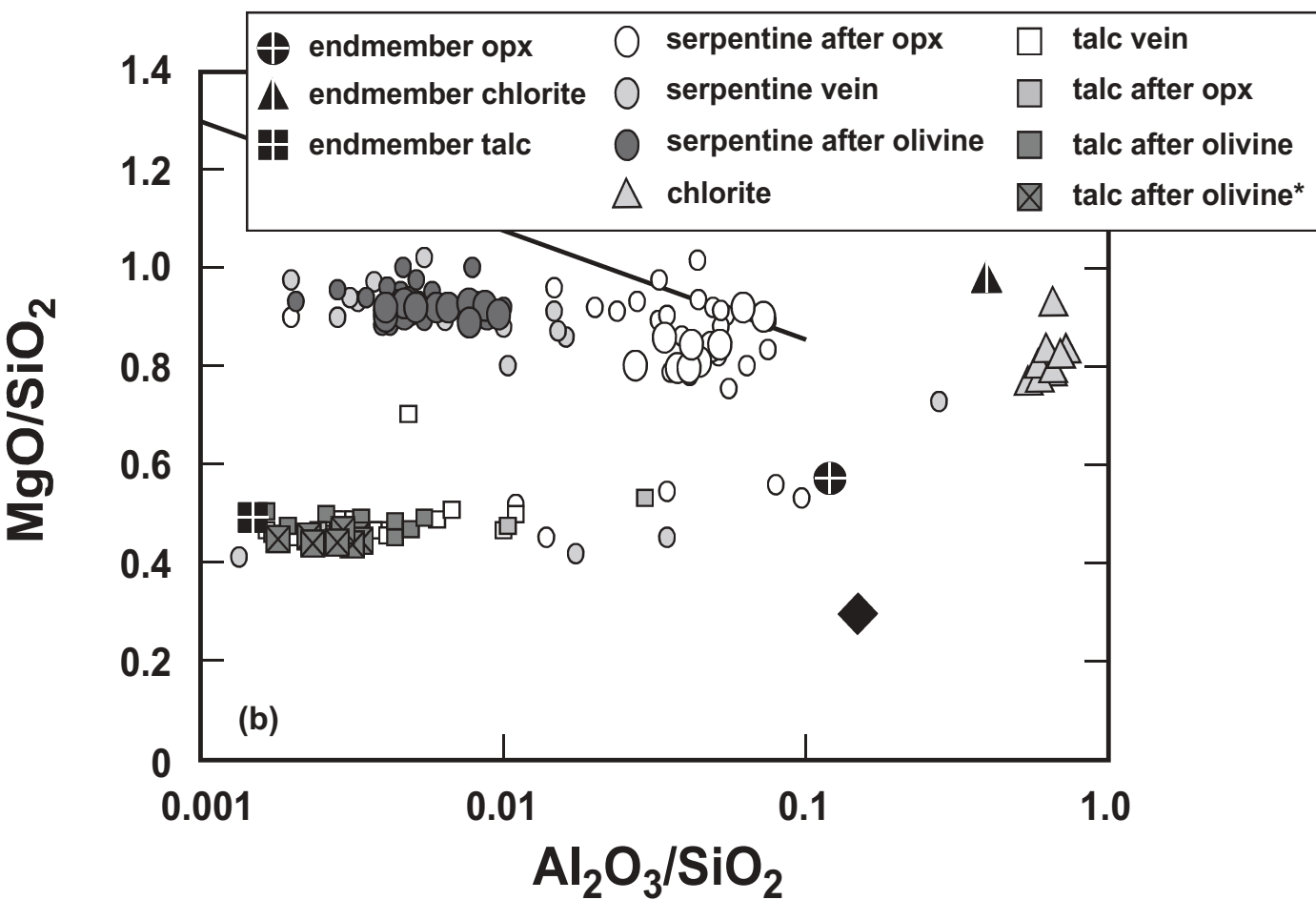
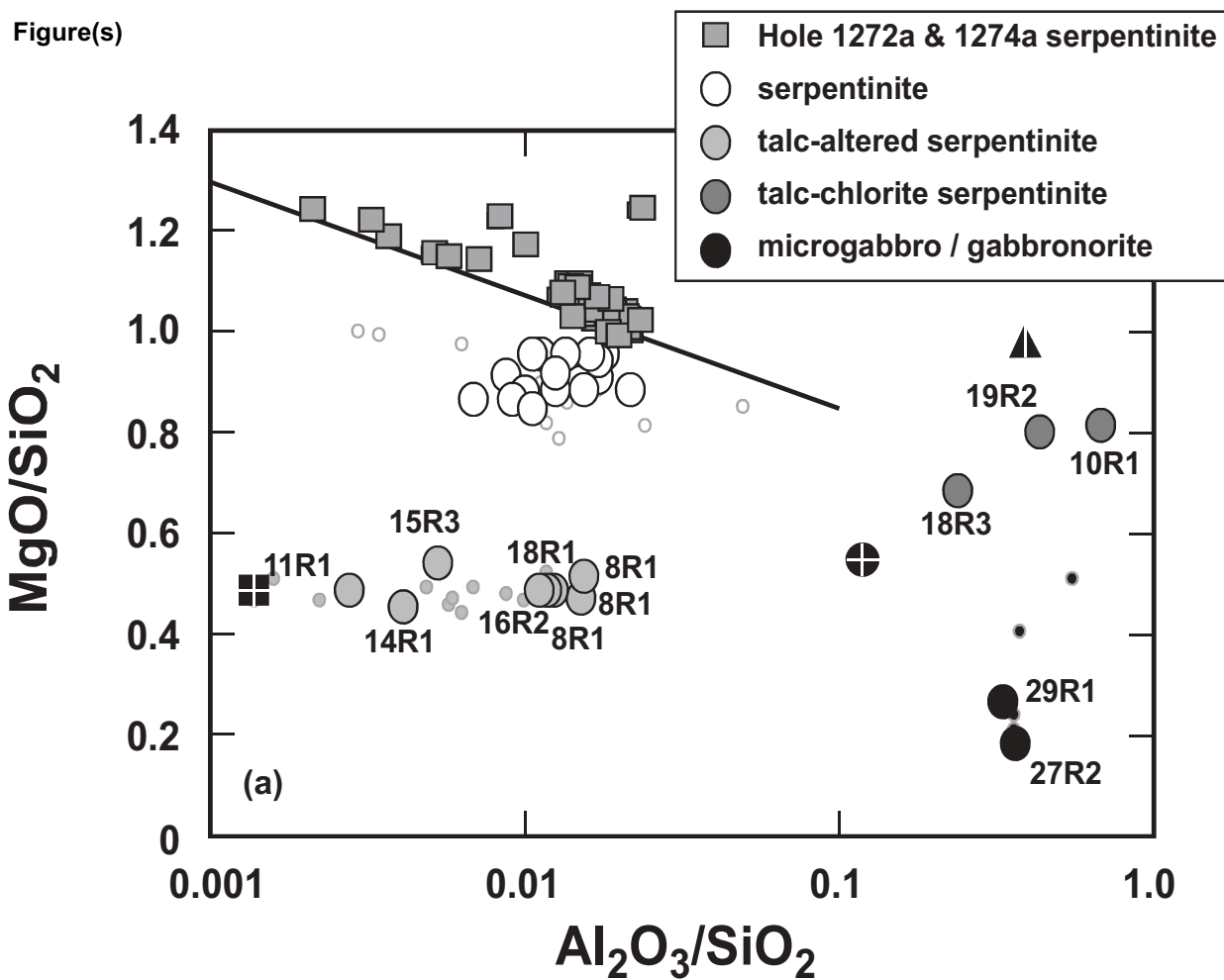
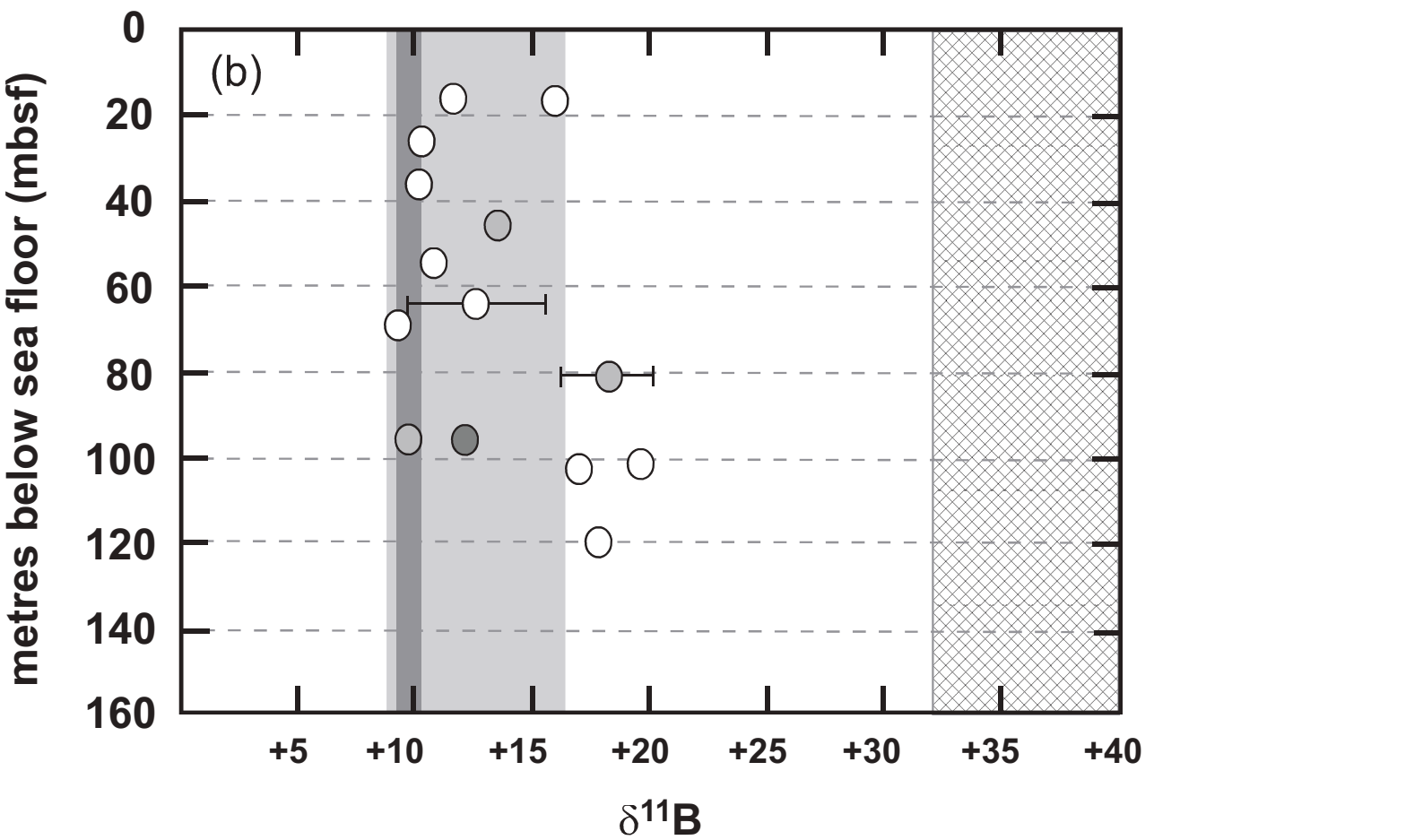
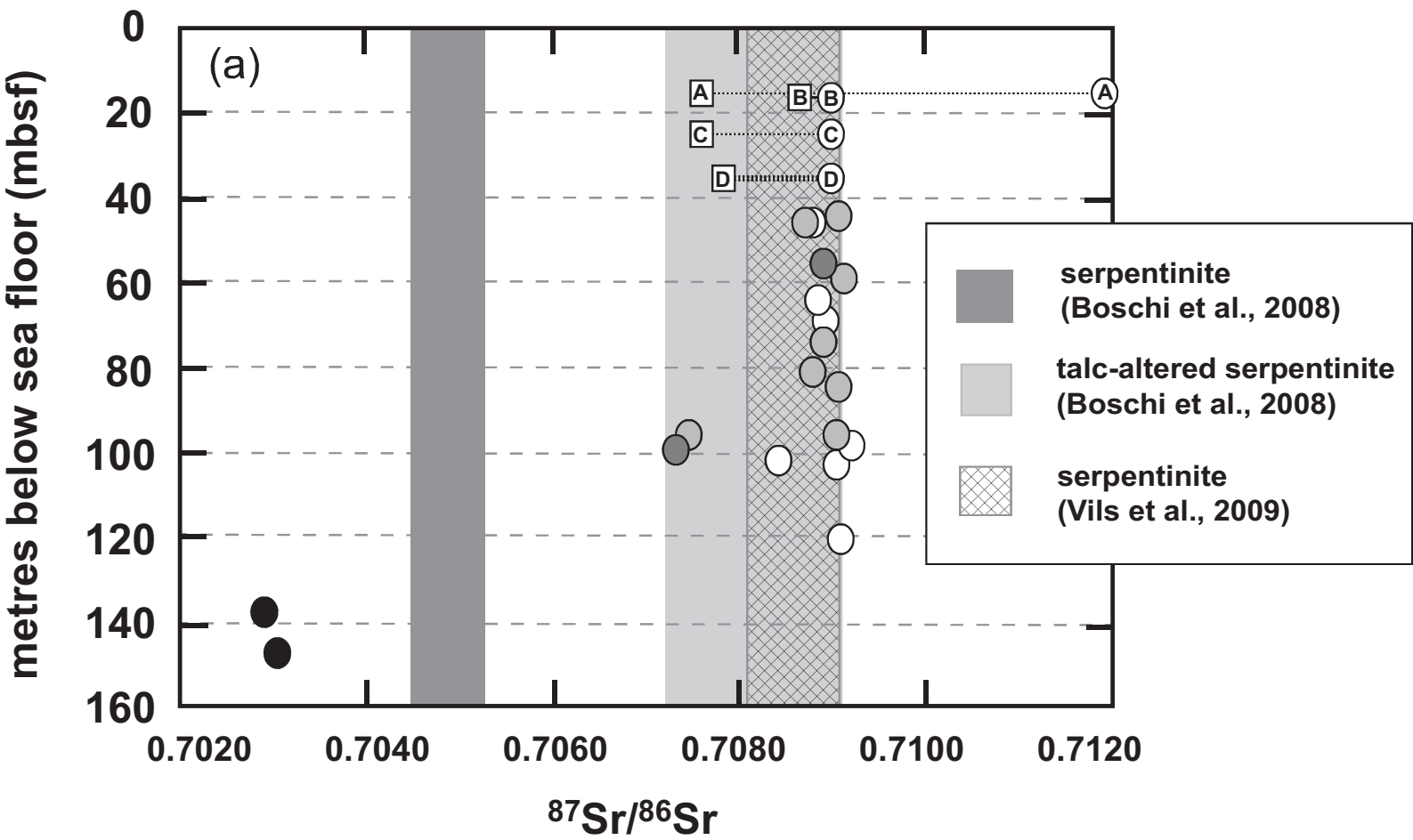
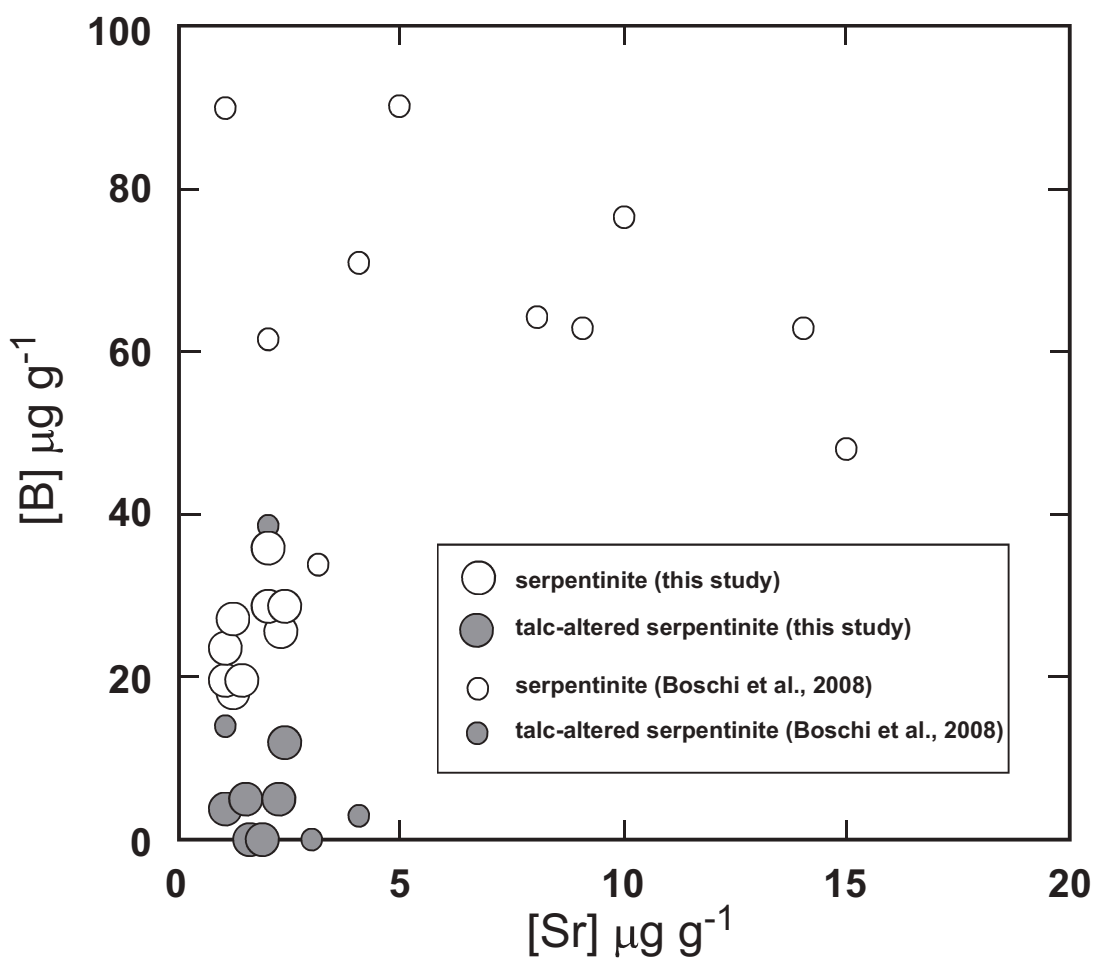


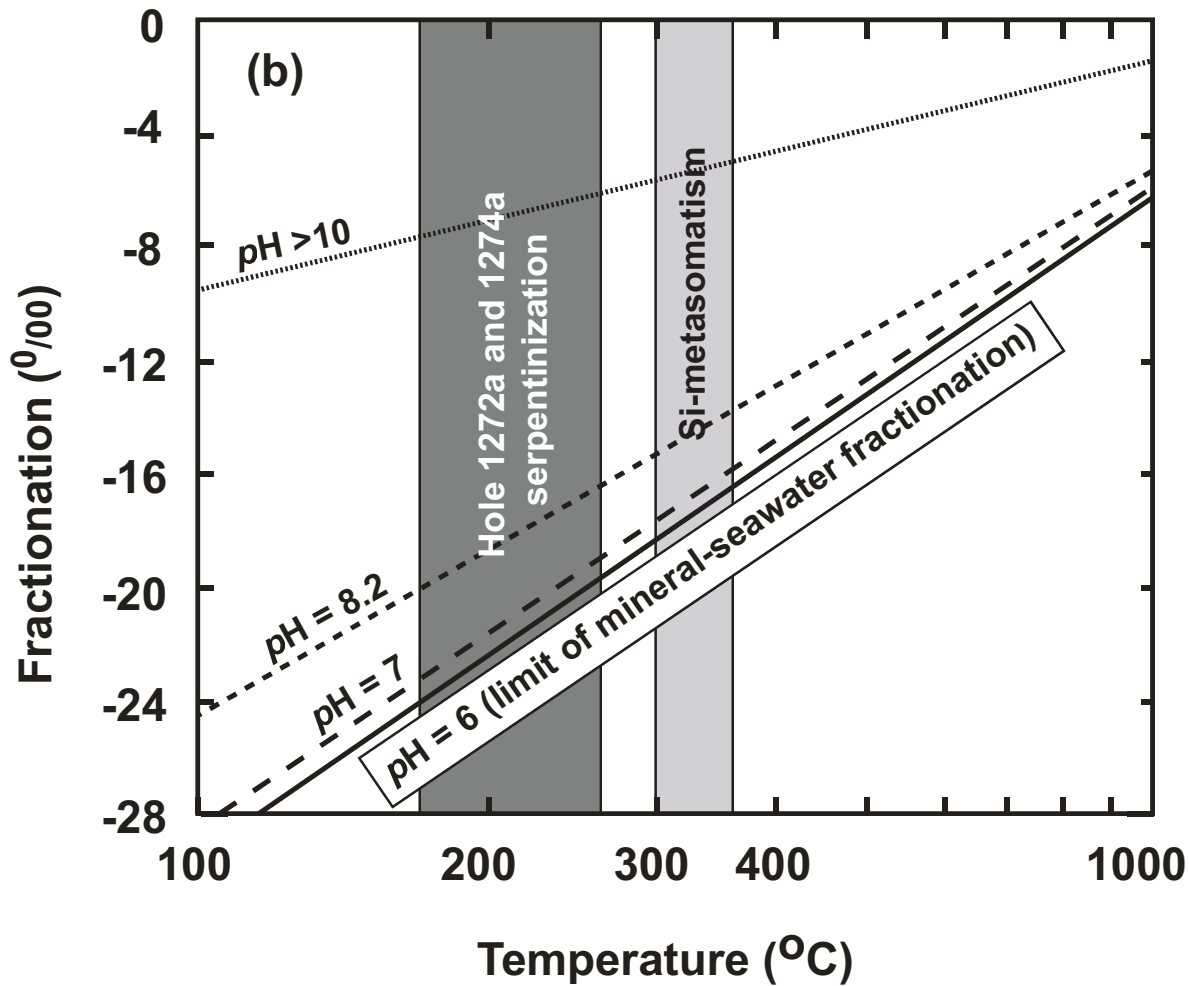
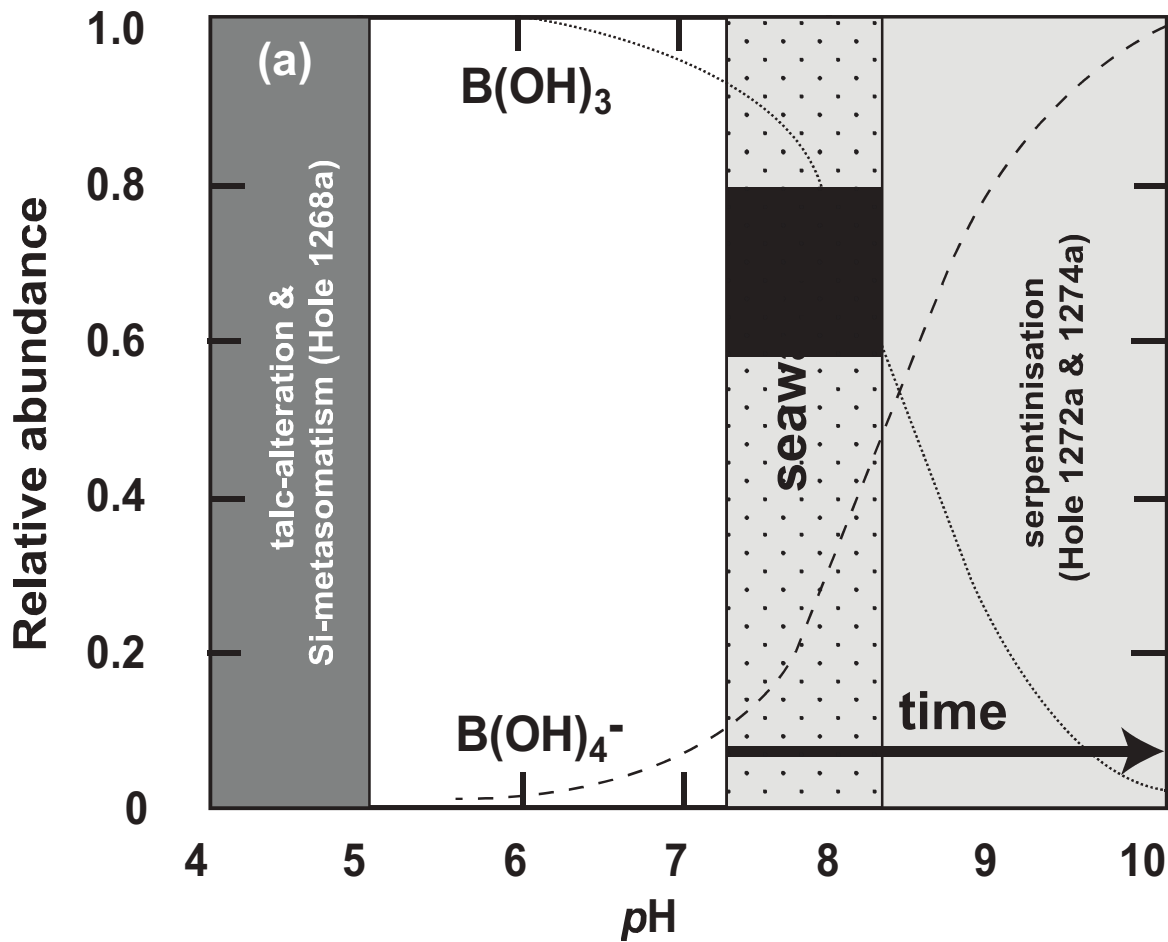
Figure 3





Figure(s)

Figure 6



Figure(s)

$\delta^{11}\text{B}$ (‰)

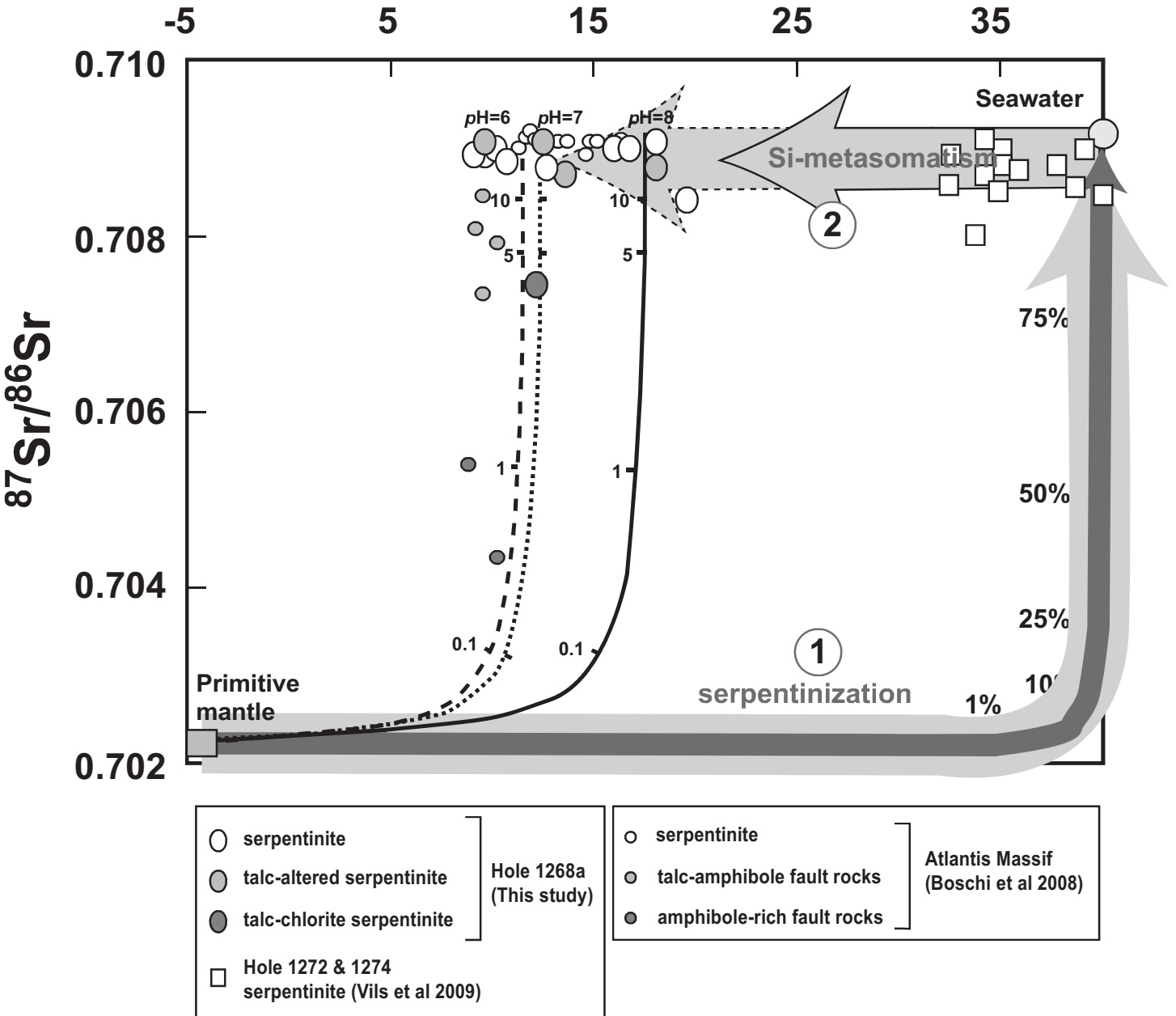


Figure 7